

# Neutrino Spectral Pinching in 3D Core-Collapse Supernovae: Late-Time Convergence, Failed-Explosion Signatures, and Viewing-Angle Dispersion

Nicolás Viaux M.<sup>1,2,\*</sup>

<sup>1</sup>*Departamento de Física, Universidad Técnica Federico Santa María, Casilla 110 V, Valparaíso, Chile*

<sup>2</sup>*Millennium Institute for Subatomic physics at high energy frontier (SAPHIR), Santiago, Chile*

(Dated: March 11, 2026)

We present a systematic survey of the neutrino spectral pinching parameter  $\alpha_p(t, M, \hat{n})$  across the Princeton FORNAX ensemble of 3D core-collapse supernova simulations. We aim to characterize the secular evolution of  $\alpha_p$  with progenitor mass and post-bounce time, describe the spectral behavior observed in the two BH-forming models of the ensemble, quantify viewing-angle systematics for terrestrial detectors, and compute oscillation-corrected detection rates for next-generation experiments.

We analyze 25 simulations spanning progenitor masses 8.1–100  $M_\odot$  with durations up to 8.47 s post-bounce, computed with the FORNAX code and the SFHo equation of state. The pinching parameter  $\alpha_p = (2\langle E \rangle^2 - E_{\text{rms}}^2)/(E_{\text{rms}}^2 - \langle E \rangle^2)$  is derived from 12-bin spectral moments on a  $128 \times 256$  sky grid for three neutrino species, enabling time- and angle-resolved spectral characterization.

Four results emerge from this survey. (1) The  $\bar{\nu}_e$  pinching floor is  $\alpha_p = 1.92 \pm 0.10$  ( $N = 13$  long-running models), lying 0.2–0.4 below 1D predictions due to 3D PNS convection. (2) Both BH-forming models (12.25, 14  $M_\odot$ ) show anti-pinching ( $\alpha_p \lesssim 0.9$ ) before collapse, with deficit  $\Delta\alpha_p \approx 0.65$  visible from  $t = 0.5$  s. (3) Two of six long-running models exhibit a hierarchy reversal ( $\langle E_{\nu_e} \rangle > \langle E_{\nu_x} \rangle$ ) after  $t = 5$  s; leptonic flavors carry  $(40 \pm 3)\%$  of radiated energy. (4) The LESA dipole is suppressed by  $\gtrsim 3\times$  in BH-forming models; viewing-angle spread  $\Delta\alpha_p^{68\%} \approx 0.8\text{--}1.5$  dominates the spectral-inversion uncertainty. Mollweide sky maps of  $L(\hat{n})$ ,  $\langle E \rangle(\hat{n})$ , and  $\alpha_p(\hat{n})$  reveal coherent angular structures driven by LESA and higher-order multipoles, with  $\alpha_p$  anticorrelated with luminosity and correlated with mean energy.

Detection rates at Hyper-Kamiokande, DUNE, JUNO, and IceCube yield 8–12% NMO/IMO discrimination during Kelvin–Helmholtz cooling. The spectral pinching parameter and the LESA dipole are established as complementary diagnostics for next-generation neutrino observatories. The late-time  $\bar{\nu}_e$  pinching floor  $\alpha_p^{\bar{\nu}_e} = 1.92 \pm 0.10$  represents the first 3D characterization of spectral convergence during Kelvin–Helmholtz cooling, lying 0.2–0.4 below 1D predictions and providing a quantitative spectral benchmark whose departures from the mean-field limit are a direct signature of 3D PNS convective transport.

## I. INTRODUCTION

The gravitational collapse of a massive star’s iron core converts approximately  $3 \times 10^{53}$  erg of gravitational binding energy into neutrinos over a timescale of tens of seconds [5, 15, 57]. This enormous neutrino luminosity ( $L_\nu \sim 10^{53}$  erg s<sup>−1</sup>) drives the supernova shock revival via neutrino heating [5, 8, 29, 44] and simultaneously encodes the thermodynamic state of the proto-neutron star (PNS), including the nuclear equation of state, lepton fraction gradients, and the efficiency of convective transport in dense matter [35, 53, 62].

A central observable of the neutrino burst is the energy spectrum of each flavor. The spectrum evolves through three distinct phases: (i) the neutronization burst at core bounce, when  $\nu_e$  alone peaks for  $\sim 20$  ms; (ii) the accretion phase, when the stalled shock drives a quasi-steady flux at  $L \sim 10^{52}$  erg s<sup>−1</sup> for  $\sim 0.2\text{--}0.5$  s; and (iii) the Kelvin–Helmholtz cooling phase, during which the PNS radiates its residual thermal energy over  $\sim 10\text{--}30$  s [9, 26, 53].

The spectral *shape* is commonly parametrized by the pinching parameter  $\alpha_p$ , defined by the quasi-thermal (or “ $\alpha$ -fit”) distribution:

$$f(E; \langle E \rangle, \alpha_p) \propto \left( \frac{E}{\langle E \rangle} \right)^{\alpha_p} \exp \left[ -(\alpha_p + 1) \frac{E}{\langle E \rangle} \right], \quad (1)$$

where  $\alpha_p$  is a dimensionless spectral-shape parameter that quantifies how narrowly the neutrino energy distribution is peaked around its mean  $\langle E \rangle$ : larger  $\alpha_p$  corresponds to a more sharply concentrated (“pinched”) spectrum with suppressed high- and low-energy tails, while smaller  $\alpha_p$  corresponds to a broader, more non-thermal distribution with enhanced tails. Concretely,  $\alpha_p = 2$  recovers a Maxwell–Boltzmann spectrum,  $\alpha_p \approx 2.3$  corresponds to a Fermi–Dirac distribution with zero chemical potential, and  $\alpha_p > 2.3$  (“pinching”) signals a spectrum narrower than Fermi–Dirac, as arises when the neutrinosphere opacity sharpens the decoupling layer [34, 65]. Values  $\alpha_p < 2$  (“anti-pinching”) indicate a distribution broader than Maxwell–Boltzmann, as can occur when a hard non-thermal tail from late-time accretion contributes to the spectrum. In core-collapse supernovae,  $\alpha_p$  evolves from moderately pinched values ( $\approx 2.3\text{--}3.5$ ) during the accretion phase toward lower values during Kelvin–Helmholtz cooling as 3D convection within the

\* nicolas.viaux@usm.cl

proto-neutron star broadens the spectral formation region.

The physical importance of  $\alpha_p$  is threefold. First, the inverse-beta-decay event rate at water-Cherenkov detectors scales as  $\langle E^2 \rangle \propto (\alpha_p + 2)/(\alpha_p + 1)$ , so a shift  $\Delta\alpha_p \approx 0.3$  alters predicted rates by  $\sim 4\text{--}6\%$ —hundreds of events at Hyper-Kamiokande for a Galactic supernova at 10 kpc—directly affecting equation-of-state and neutron-star-mass inference [36, 63]. Second, the boundaries of collective-oscillation spectral swaps and the onset of fast-flavor instabilities are controlled by the spectral widths of  $\nu_e$  and  $\bar{\nu}_e$ , so  $\alpha_p$  sets the post-oscillation spectra reaching terrestrial detectors and governs the detectability of the neutrino mass ordering [17, 20, 60]. Third, charged-current captures in the neutrino-driven wind depend on the high-energy spectral tail; spectral pinching suppresses this tail, reducing the electron fraction  $Y_e$  and shifting conditions for  $r$ -process nucleosynthesis [26, 55, 59]. The  $\alpha_p$  floor derived in this work therefore provides a simulation-motivated anchor for all three of these applications.

The  $\sim 24$  events from SN 1987A remain the only direct measurement of the supernova neutrino burst, and subsequent analyses have constrained  $\langle E_{\bar{\nu}_e} \rangle$  and  $\alpha_p$  through fits to the Kamiokande-II, IMB, and Baksan data [33, 57]. Those fits are degenerate between spectral mean and shape, and the adopted prior on  $\alpha_p$  materially affects the inferred mean energy and total radiated energy. The 3D floor established here provides a simulation-motivated prior for such analyses. For the next Galactic event, next-generation detectors will accumulate  $\mathcal{O}(10^4)$  events enabling per-bin spectral measurements, so accurate spectral templates with realistic  $\alpha_p$  uncertainties will be essential for equation-of-state constraints and tests of non-standard neutrino physics [17, 36].

Despite this importance, no systematic study of  $\alpha_p(t, M)$  across a large, homogeneous ensemble of 3D simulations has been performed. 1D models [23, 26, 53] predict a cooling-phase floor near  $\alpha_p \approx 2.0\text{--}2.3$ . In 2D, convection inside the PNS slightly broadens spectra [37, 43]. In 3D, additional symmetry-breaking instabilities — the standing accretion shock instability [SASI; 66] and the lepton-number emission self-sustained asymmetry [LESA; 49, 67] — a persistent hemispheric asymmetry in  $\nu_e/\bar{\nu}_e$  emission quantified by its dipole amplitude  $\varepsilon$  (defined precisely in Eq. 11) — modulate spectral moments at the  $\lesssim 10\%$  level, but the secular time- and angle-averaged spectral evolution across a wide progenitor mass range remains uncharacterized.

With 25 models spanning  $8.1$  to  $100 M_\odot$  and simulation durations reaching up to  $8.47$  s post-bounce, the Princeton FORNAX dataset [16, 72] provides the homogeneous, long-duration 3D ensemble needed to characterize the mass and time dependence of  $\alpha_p$ . Choi et al. [14] analyzed luminosities, mean energies, and multi-detector event rates from this dataset, but did not study  $\alpha_p$ . In the present work we analyze the 25 models for which full angle-resolved output is available, spanning  $8.1\text{--}100 M_\odot$ ;

all spectral quantities are derived directly from the 12-bin spectral data rather than from the angle-averaged moment files.

The paper is organized as follows. Section II describes the simulations and data. Section III defines  $\alpha_p$  and the analysis procedure. Section IV presents the results. Section V discusses observational prospects. Section VI interprets results and places them in context. Section VII presents our conclusions.

## II. SIMULATIONS AND DATA

### A. The Princeton Fornax Code

All simulations were performed with FORNAX, a multi-dimensional radiation-hydrodynamics code developed at Princeton University [56, 61]. The code solves the *two-moment* (M1) neutrino transport equations coupled to compressible hydrodynamics on a spherical-polar grid.

FORNAX solves the two-moment (M1) neutrino transport equations for three species ( $\nu_e$ ,  $\bar{\nu}_e$ ,  $\nu_x$ ) coupled to compressible hydrodynamics on a spherical-polar grid. The system is closed by the Minerbo [41] maximum-entropy prescription, whose Eddington factor interpolates between the diffusion ( $f = 1/3$ ) and free-streaming ( $f = 1$ ) limits. The M1 scheme overestimates the tangential radiation pressure in the semi-transparent regime relative to full Boltzmann transport [31], but reproduces angle-averaged spectral moments to  $\lesssim 5\%$  accuracy compared to variable-Eddington-factor codes during the accretion phase [48]; systematic differences in the cooling phase remain to be quantified by long-duration cross-code comparisons (Section VIA).

Gravity employs the pseudo-Newtonian effective potential of Marek et al. [38], which reproduces the GR deepening of the gravitational well critical for accurate PNS cooling [10, 37]; the approximation becomes inaccurate only in the final  $\lesssim 10$  ms before BH formation, well before the spectral features we characterize (Section IV D). Interaction rates include charged-current absorption and emission for  $\nu_e$  and  $\bar{\nu}_e$ ; neutral-current scattering off nucleons, nuclei, and electrons; thermal pair processes; and nucleon–nucleon bremsstrahlung [6, 11, 24]. The nuclear EOS is SFHo [62] ( $n_0 = 0.1595 \text{ fm}^{-3}$ ,  $K = 245 \text{ MeV}$ ,  $R_{1.4} = 11.9 \text{ km}$ ,  $M_{\text{max}} \approx 2.05 M_\odot$ ). Full algorithmic details are given in Skinner et al. [61].

### B. Model Suite

Appendix Table I lists the 25 progenitor models analyzed in this work (angle-resolved subset). ZAMS masses span  $8.1\text{--}100 M_\odot$ , sampling a broad range of iron-core compactness. The compactness parameter [50],

$$\xi_{2.5} = \frac{2.5 M_\odot / M_\odot}{R(M = 2.5 M_\odot) / 1000 \text{ km}}, \quad (2)$$

quantifies how concentrated the stellar interior is at a mass coordinate of  $2.5 M_\odot$ . Models above the BH-formation transition range  $\xi_{2.5} \approx 0.3\text{--}0.45$  [50, 64] form BHs with high probability; the two failed models in our sample ( $12.25 M_\odot$  and  $14 M_\odot$ ) have  $\xi_{2.5} = 0.458$  and  $0.528$ , placing them clearly above this range. We adopt the  $\xi_{2.5}$  definition of O’Connor & Ott [50] for consistency with the Fornax publications that report this quantity for the models studied here. Choi et al. [14] employ  $\xi_{1.75}$ , which has been argued to provide better discrimination near the BH-formation boundary [2]; the two compactness parameters are correlated and our qualitative conclusions are independent of this choice. We note that Choi et al. [14] discuss additional high-mass models (e.g., 40 and  $60 M_\odot$ ) that achieve brief shock revival but are susceptible to later fallback; in our 25-model sample, only 12.25 and  $14 M_\odot$  reach BH formation (PNS mass exceeding  $\approx 2.05 M_\odot$ , the SFHo maximum) without achieving a sustained explosion.

Progenitors were drawn from Sukhbold et al. [64] (solar metallicity,  $9\text{--}100 M_\odot$ ) and Woosley & Heger [79] (low-mass models  $8.1$  and  $9.6 M_\odot$ ). Simulation durations range from  $\sim 0.43$  s ( $100 M_\odot$ , partial run) to  $8.47$  s ( $18 M_\odot$ ).

### C. Data Products

For each model and species  $s \in \{0 : \nu_e, 1 : \bar{\nu}_e, 2 : \nu_x\}$ , the spectral data files [72] provide time series of: the post-bounce time  $t$  [s]; the angle-averaged luminosity  $L_s$  [ $\times 10^{51}$  erg s $^{-1}$ ]; the mean energy  $\langle E_s \rangle$  [MeV]; the RMS energy  $E_{\text{rms},s} = \sqrt{\langle E_s^2 \rangle}$  [MeV]; and a skewness energy  $E_{\text{skw},s}$  [MeV]. The  $\nu_x$  entries represent the sum over all four heavy-lepton flavors ( $\nu_\mu, \nu_\tau$  and their antiparticles). The median temporal resolution is  $\sim 1$  ms. In this work,  $\alpha_p$  is computed directly from the angle-averaged 12-bin spectral moments (Eq. 4), with no quasi-thermal approximation. Appendix Table II demonstrates this for representative models (11, 17,  $18.5 M_\odot$ ): the moment-based value is exact (0% difference) since both use the same spectral bins.

The pinching parameter computed via Eq. (4) is an *effective* spectral-shape measure derived from only the first two energy moments ( $\langle E \rangle$  and  $E_{\text{rms}}^2 \equiv \langle E^2 \rangle$ ). It is *not* a best-fit parameter to the full binned spectrum. Specifically,  $\alpha_p^{\text{mom}}$  would reproduce the true best-fit  $\alpha_p$  exactly if and only if the spectrum belongs strictly to the quasi-thermal family (Eq. 3). For real neutrino spectra with non-thermal contributions (e.g., hard-tail accretion luminosity), the two can differ; in particular, anti-pinching ( $\alpha_p < 2$ ) in the BH-forming models manifests as a genuine increase in  $E_{\text{rms}}^2/\langle E \rangle^2$  regardless of whether the underlying distribution is strictly quasi-thermal. M1 spectral moments agree with variable-Eddington-factor moments at the  $\lesssim 5\text{--}10\%$  level during the accretion phase [66]; systematic differences in the cooling phase remain to be quantified.

## III. METHODS

### A. The Quasi-Thermal Spectral Parametrization

We employ the quasi-thermal family introduced by Keil et al. [34] and widely used in detection and oscillation studies [36, 60, 65]:

$$f(E; \langle E \rangle, \alpha_p) = \mathcal{N} \left( \frac{E}{\langle E \rangle} \right)^{\alpha_p} \exp \left[ -\frac{(\alpha_p + 1)E}{\langle E \rangle} \right], \quad (3)$$

where  $\mathcal{N}$  is fixed by  $\int_0^\infty f(E) dE = 1$ .

The  $n = 2$  moment of distribution (3) gives  $\langle E^2 \rangle = [(\alpha_p + 2)/(\alpha_p + 1)]\langle E \rangle^2$ . Defining  $E_{\text{rms}} \equiv \sqrt{\langle E^2 \rangle}$  (used interchangeably with  $E_{\text{rms}}^2 \equiv \langle E^2 \rangle$  throughout), inverting yields:

$$\alpha_p = \frac{2\langle E \rangle^2 - E_{\text{rms}}^2}{E_{\text{rms}}^2 - \langle E \rangle^2}, \quad (4)$$

valid for any distribution with  $E_{\text{rms}}^2 > \langle E \rangle^2$ . The normalized variance  $\sigma_E^2 \equiv (\langle E^2 \rangle - \langle E \rangle^2)/\langle E \rangle^2 = 1/(\alpha_p + 1)$  [34]; Appendix Table III lists reference values.

The physical interpretation of  $\alpha_p$  is the following. A value  $\alpha_p = 2$  corresponds to a Maxwell–Boltzmann spectrum;  $\alpha_p \approx 2.3$  to a Fermi–Dirac distribution with zero chemical potential; and  $\alpha_p > 2.3$  (“pinching”) to spectra narrower than Fermi–Dirac, as expected when neutrinos decouple from a hot, optically thick neutrinosphere where thermalization is efficient. Values  $\alpha_p < 2$  (“anti-pinching”) correspond to distributions broader than Maxwell–Boltzmann, indicative of a hard non-thermal tail from accretion or of a flattened temperature gradient at the decoupling surface. In core-collapse supernovae,  $\alpha_p$  is important because it governs the cross-section-weighted event rate at terrestrial detectors (through the  $\sigma \propto E^2$  weighting), sets the effective spectral input for flavor-transformation calculations, and encodes the thermodynamic state of the PNS interior: the degree of spectral pinching is set by the temperature gradient at the neutrinosphere, making  $\alpha_p$  a direct probe of PNS convective transport and cooling physics.

### B. Quality Cuts and Smoothing

Raw  $\alpha_p(t)$  traces exhibit short-timescale ( $\lesssim 10$  ms) fluctuations driven by convective turnover inside the PNS (overtake timescale  $\tau_{\text{conv}} \sim 20$  ms) and by numerical noise at the level of  $|\delta\alpha_p| \lesssim 0.1$ . We apply a 25 ms boxcar rolling mean, which preserves features on timescales  $\gtrsim 50$  ms while suppressing shot noise. The window corresponds to approximately twice the SASI turnover timescale ( $\tau_{\text{SASI}} \sim 10\text{--}20$  ms at early times, rising to  $\sim 50$  ms during the cooling phase; Tamborra et al. 66), ensuring that random-phase SASI fluctuations are averaged over without erasing the secular spectral trends we characterize. We discard samples where

$E_{\text{rms}}^2 - \langle E \rangle^2 < 0.01 \text{ MeV}^2$  or  $\alpha_p < -0.5$  (less than 0.4% of all time steps). These cuts are triggered almost exclusively during the neutronization burst ( $t \lesssim 10 \text{ ms}$ , where the  $\nu_e$  spectral variance temporarily collapses as the burst narrows the spectrum) and at the final time step of the two BH-forming models immediately before the luminosity cutoff. No cut is triggered at any epoch relevant to the pre-BH anti-pinching trajectory ( $t = 0.3\text{--}2.7 \text{ s}$ ), confirming that the quality filter does not affect the BH spectral evolution (Section IV D).

**Smoothing convention.** Unless stated otherwise, all scalar time-series quantities quoted in this paper (spectral survey curves, Spearman correlations, floor estimate, Spearman  $r_S$  values, and  $f_+$ ) are computed on the smoothed series. The late-time floor value (Section IV B) is computed as the mean of per-model time-averages over  $t = 3.0 \text{ s} - t_{\text{max}}$  after smoothing, restricted to the  $N = 13$  models with  $t_{\text{max}} > 3.5 \text{ s}$ ; the Spearman coefficients use single smoothed values at the target epoch; and  $f_+$  uses a 250 ms boxcar applied after the primary 25 ms smoothing. The viewing-angle percentile bands in Section IV F 2 are computed directly from the unsmoothed sky map at a single snapshot epoch.

### C. Progenitor-Mass Interpolation and Total Energy

To connect individual model values at a fixed epoch into a continuous function of progenitor mass, we fit a degree- $k$  B-spline ( $k = \min(2, N - 1)$ ) on the  $\log_{10}(M/M_\odot)$  axis [18]; the 9a/9b duplicate is averaged before spline construction. The total radiated energy per species is  $E_s = \int_0^{t_{\text{max}}} L_s dt$  (trapezoidal rule, native  $\sim 1 \text{ ms}$  grid), and  $E_{\text{tot}} = E_{\nu_e} + E_{\bar{\nu}_e} + E_{\nu_x}$  with  $E_{\nu_x}$  summing all four heavy-lepton flavors.

## IV. RESULTS

### A. Neutrino Luminosity Survey

The luminosity evolution  $L_s(t)$  for all 25 models, grouped by explosion outcome and mass regime, is presented in Fig. 1.

All three species follow the same qualitative evolution: a bright neutronization burst in  $\nu_e$  alone, a  $\sim 10^{52} \text{ erg s}^{-1}$  accretion plateau, and a power-law Kelvin–Helmholtz decay. During the cooling phase, the luminosity follows

$$L_s(t) \approx L_{s,0} \left( \frac{t}{t_0} \right)^{-n_s}, \quad (5)$$

with cooling index  $n_s \approx 1.4$  for  $\bar{\nu}_e$  in the range  $3 \text{ s} \lesssim t \lesssim 8 \text{ s}$ , consistent with diffusive transport through the PNS mantle [54]. The Kelvin–Helmholtz cooling timescale  $\tau_{\text{KH}} \sim 10\text{--}30 \text{ s}$  is set by the ratio of residual thermal energy to luminosity [35, 53]. The two BH-forming models

terminate with a luminosity cutoff when the PNS accretes past  $M_{\text{max}} \approx 2.05 M_\odot$  (SFHo EOS; Steiner et al. 62).

Higher-mass progenitors sustain higher luminosities for longer, consistent with larger PNS masses and binding energies  $E_b \approx (2.4\text{--}3.4) \times 10^{53} \text{ erg}$  [35].

### B. Spectral Pinching Survey

The spectral pinching parameter  $\alpha_p(t)$  for all 25 models, computed from the angle-averaged moments, is presented in Fig. 2.

#### 1. General Trends

During the accretion phase ( $t_{\text{pb}} \lesssim 0.5 \text{ s}$ ), the  $\nu_e$  spectrum is most pinched ( $\alpha_p^{\nu_e} \approx 2.5\text{--}3.5$ ), followed by  $\bar{\nu}_e$  ( $\approx 2.2\text{--}3.0$ ) and  $\nu_x$  ( $\approx 2.0\text{--}2.8$ ). This ordering reflects different optical depths at decoupling. In the diffusion approximation, the ratio  $E_{\text{rms}}/\langle E \rangle$  at the neutrinosphere satisfies

$$\frac{E_{\text{rms}}^2}{\langle E \rangle^2} \approx 1 + \frac{1}{\alpha_p + 1} = \frac{\alpha_p + 2}{\alpha_p + 1}, \quad (6)$$

so that a higher optical depth (deeper, hotter sphere) corresponds to a value of  $E_{\text{rms}}/\langle E \rangle$  closer to the Planck limit of  $\sim 1.22$ , i.e., a higher  $\alpha_p$ .

After shock revival,  $\alpha_p$  declines for all species as the neutrinosphere contracts and the temperature gradient at decoupling flattens. The  $\bar{\nu}_e$  pinching reaches a consistent empirical floor among the 13 models that extend beyond  $t = 3 \text{ s}$  (models 11, 15.01, 16, 17, 18, 18.5, 19, 19.56, 20, 23, 24, 25, 60  $M_\odot$ ):

$$\alpha_p^{\bar{\nu}_e} \Big|_{t_{\text{pb}} > 3 \text{ s}} = 1.92 \pm 0.10 \text{ (scatter)}, \quad \sigma_{\text{mean}} = 0.03, \quad N = 13. \quad (7)$$

We emphasize that the  $\pm 0.10$  is the *model-to-model scatter* (standard deviation), not the uncertainty on the mean; the standard error on the mean is  $0.10/\sqrt{13} \approx 0.03$ . The distribution is also characterized by: median = 1.88, with a 16–84% inter-model range of [1.83, 2.01], indicating modest model-to-model variation. The slight right skew (mean > median) is driven by the two or three models with  $\alpha_p^{\text{floor}} \approx 2.0\text{--}2.01$ ; inspection reveals these are the 60  $M_\odot$  and 25  $M_\odot$  runs, which have shorter cooling-phase durations ( $t_{\text{max}} \lesssim 4.5 \text{ s}$ ) and may not have fully relaxed to the late-time floor. The value lies  $\sim 0.1\text{--}0.4$  below 1D predictions of  $\approx 2.0\text{--}2.3$  [26], attributable to 3D PNS convection broadening the spectrum [43, 59].

#### 2. Mass Dependence at Fixed Epoch

The mass dependence of  $\alpha_p$  at three post-bounce epochs ( $t = 0.5, 1.0, \text{ and } 3.0 \text{ s}$ ) is shown in Fig. 3.

At  $t = 0.5 \text{ s}$ , there is a *negative* correlation between progenitor mass and  $\alpha_p^{\bar{\nu}_e}$  across the full 25-model sample:

Neutrino Luminosity Evolution — Princeton/Fornax 3D Suite (25 models, 8.1–100  $M_\odot$ )

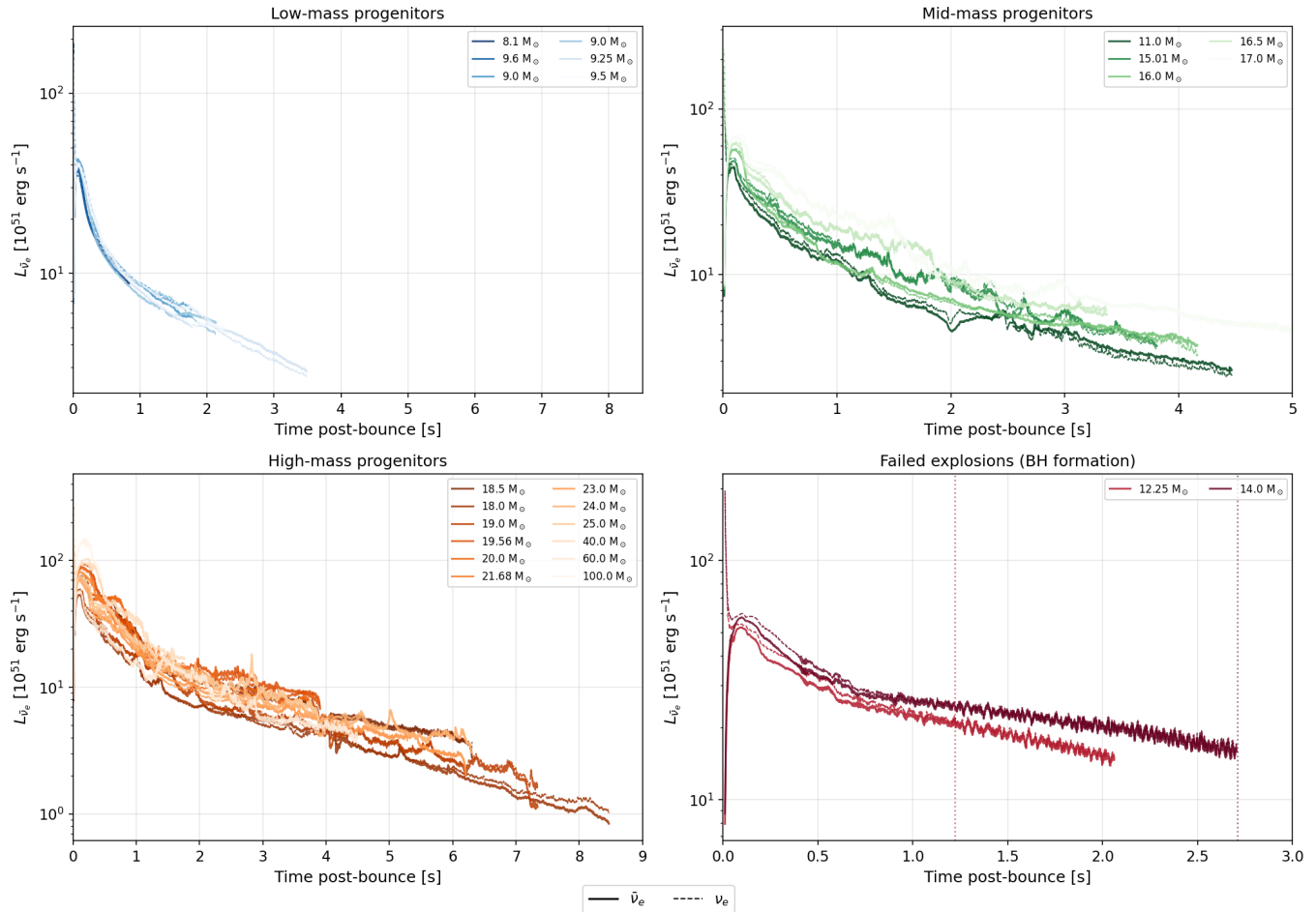


FIG. 1. Neutrino luminosity  $L_s(t)$  for all 25 FORNAX models, grouped by explosion outcome and mass regime. Colors run from light (low mass) to dark (high mass). Species:  $\nu_e$  (blue),  $\bar{\nu}_e$  (red),  $\nu_x$  (four heavy-lepton flavors; green dashed). The  $\nu_e$  neutronization burst is visible as a narrow peak at  $t \lesssim 20$  ms. The BH-forming models (bottom-right panel) terminate abruptly. The late-time power-law decay  $L \propto t^{-n}$  with best-fit index  $n \approx 1.4$  (fitted to the 17 and 18.5  $M_\odot$  runs over  $t = 2\text{--}6$  s; Eq. 5) is visible in the longest-duration models.

the low-mass models (8–10  $M_\odot$ ) develop compact neutrinospheres at early times with characteristically pinched spectra ( $\alpha_p \approx 3.3\text{--}3.4$ ), while the high-mass ( $> 20 M_\odot$ ) models show  $\alpha_p \approx 2.0\text{--}2.5$ . Quantitatively, the Spearman rank correlation coefficient between progenitor mass and  $\alpha_p^{\bar{\nu}_e}(0.5\text{ s})$  is  $r_S = -0.85$  ( $p < 0.0001$ ,  $N = 23$  successful models).

At  $t = 1.0$  s, the negative mass correlation has weakened: the Spearman coefficient drops to  $r_S = -0.71$  ( $p < 0.001$ ,  $N = 21$  models reaching this epoch), indicating that spectral differentiation by mass persists into early cooling but at reduced significance. The high-mass models ( $> 18 M_\odot$ ) show  $\alpha_p^{\bar{\nu}_e} \approx 1.8\text{--}2.2$ , while low-mass models maintain  $\approx 2.4\text{--}2.8$ .

By  $t = 3.0$  s the mass dependence of  $\alpha_p^{\bar{\nu}_e}$  is no longer significant:  $r_S = -0.40$ ,  $p = 0.14$  ( $N = 15$  models with  $t_{\text{max}} > 3$  s), i.e., we cannot reject the null hypothesis of

no mass correlation at  $> 2\sigma$ . For  $\nu_x$  the cooling-phase Spearman coefficient is  $r_S = -0.53$ ,  $p = 0.04$ , indicating a marginal negative trend with mass, but this is sensitive to the small sample of long-duration models and should not be over-interpreted.

The two BH-forming models (shaded bands,  $\xi_{2.5} = 0.458$  and  $0.528$ ; Appendix Table I) lie 0.5–0.8 below the successful-model B-spline at all three epochs, constituting a persistent spectral discriminant that precedes BH formation by  $\gtrsim 0.5\text{--}1.0$  s. At  $t = 0.5$  s, the BH models have  $\alpha_p^{\bar{\nu}_e} \approx 1.75$ , compared to  $\approx 2.41$  for the 11  $M_\odot$  neighbor and  $\approx 2.39$  for the 15.01  $M_\odot$  neighbor — a deficit of  $\Delta\alpha_p \approx 0.65$  that distinguishes them well before the luminosity shutdown.

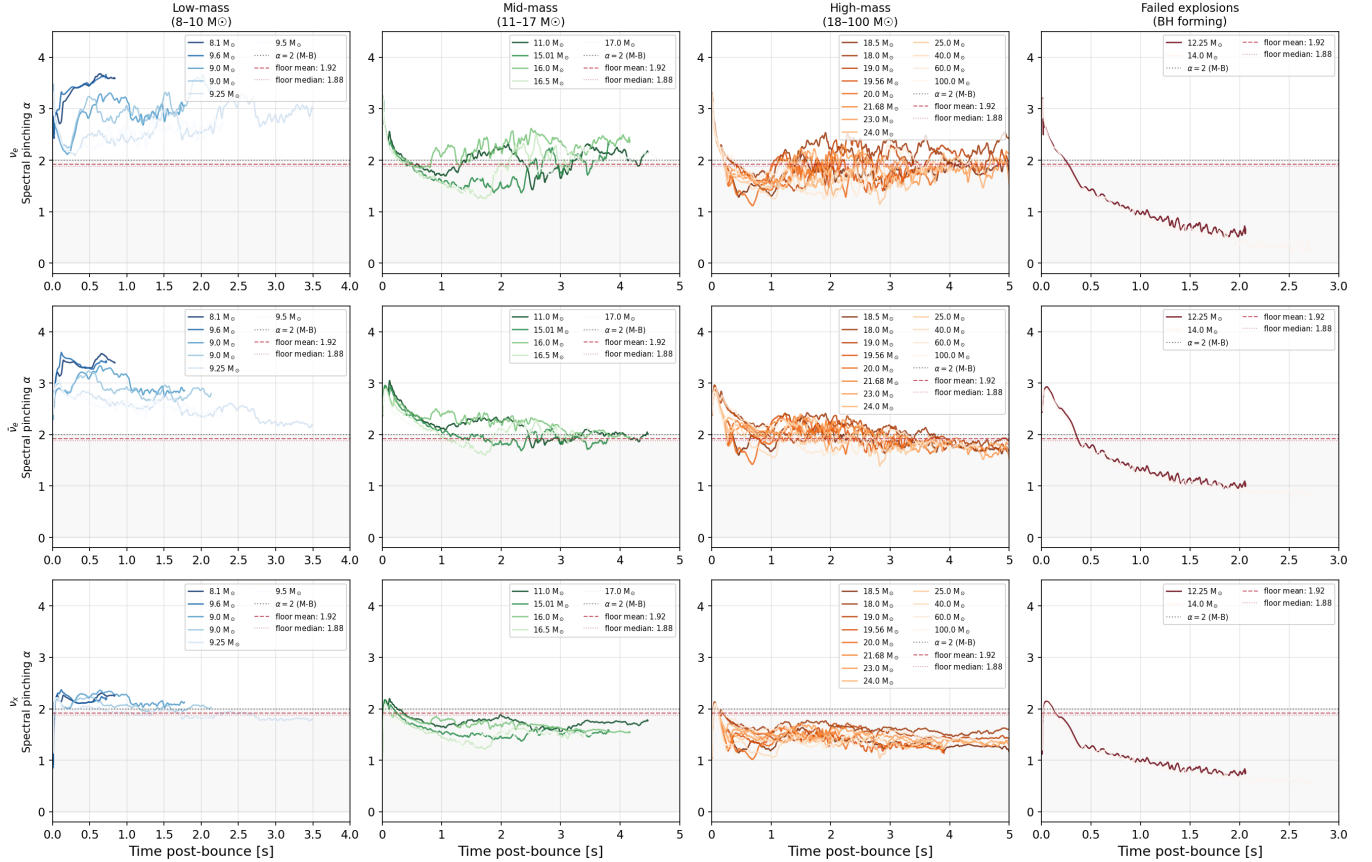
Spectral Pinching Parameter  $\alpha(t)$  — 25 Fornax 3D Models (8.1–100  $M_\odot$ )

FIG. 2. Spectral pinching parameter  $\alpha_p(t)$  for all 25 models and three neutrino species. Colors code progenitor mass (light = low mass, dark = high mass). BH-forming models ( $12.25, 14 M_\odot$ ) are in red. Gray dashed line:  $\alpha_p = 2$  (Maxwell–Boltzmann reference). A 25 ms rolling average has been applied to suppress convective fluctuations.

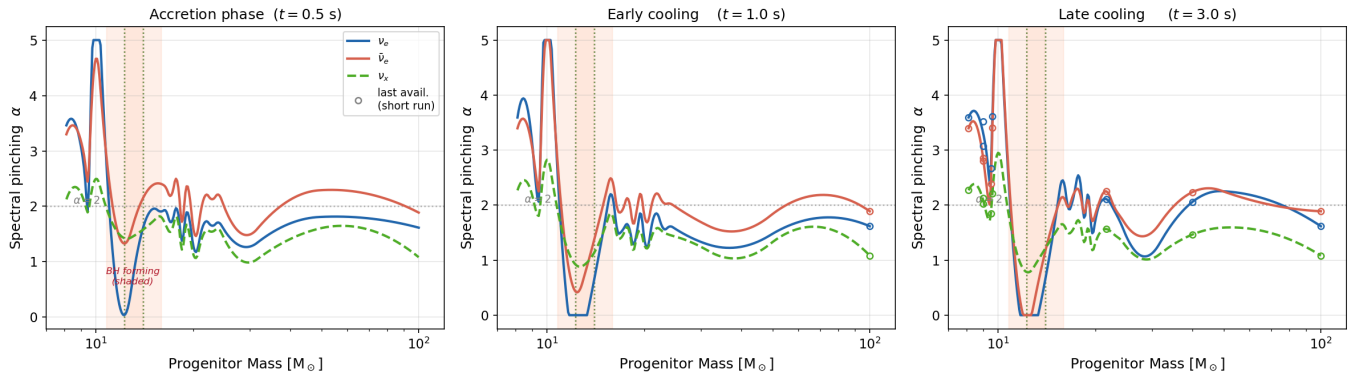
Spectral Pinching  $\alpha$  vs. Progenitor Mass — Three Evolutionary Phases (25 models)

FIG. 3. Spectral pinching  $\alpha_p$  vs. progenitor mass at three post-bounce epochs (columns). Quadratic ( $k = 2$ ) B-spline interpolation through the mass-sorted successful models for each species ( $\nu_e$ : blue,  $\bar{\nu}_e$ : orange,  $\nu_x$ : green dashed); a quadratic spline is used to suppress Runge-phenomenon oscillations at sparse mass sampling. Shaded vertical bands: BH-forming progenitors ( $12.25$  and  $14 M_\odot$ ). Gray dashed line:  $\alpha_p = 2$  (Maxwell–Boltzmann reference). Horizontal colored solid lines: late-time floor value  $\alpha_p^{\bar{\nu}_e} = 1.92$  (orange),  $\alpha_p^{\nu_e} = 2.05$  (blue), and  $\alpha_p^{\nu_x} = 2.12$  (green), averaged over the  $N = 13$  long-running models (Section IV B). The BH models lie persistently  $\sim 0.5$ – $0.8$  below the successful-model trend.

## C. Neutrino Energy Hierarchy and Late-Time Reversal

The standard energy hierarchy  $\langle E_{\nu_x} \rangle > \langle E_{\bar{\nu}_e} \rangle > \langle E_{\nu_e} \rangle$  is set by the opacity-dependent decoupling radii. For

free-streaming neutrinos above the neutrinosphere at ra-

dius  $r_\nu^{(s)}$ , the mean energy scales as  $\langle E_s \rangle \approx 3.15 T(r_\nu^{(s)})$  (Fermi–Dirac approximation), where  $T(r)$  is the matter temperature at the decoupling surface. Since charged-current opacity for  $\nu_e$  and  $\bar{\nu}_e$  scales as  $\sigma \propto E_\nu^2 Y_e \rho$  while neutral-current opacity  $\propto E_\nu^2 \rho$ ,  $\nu_x$  decouple at deeper, hotter radii during the accretion phase, giving  $\langle E_{\nu_x} \rangle > \langle E_{\bar{\nu}_e} \rangle > \langle E_{\nu_e} \rangle$  [7, 51, 58].

The mean energy evolution and hierarchy difference are shown in Fig. 4 for models running past 5 s. Throughout this section,  $\langle E_{\nu_x} \rangle$  denotes the *per-flavor* mean energy. In the FORNAX spectral data files, the  $\nu_x$  luminosity  $L_{\nu_x}$  is the *sum* over all four heavy-lepton flavors, but the mean energy  $\langle E_{\nu_x} \rangle$  is the energy-weighted spectral mean, which equals the per-flavor value by symmetry (all four heavy-lepton species carry identical spectra). Thus comparing  $\langle E_{\nu_e} \rangle$  with  $\langle E_{\nu_x} \rangle$  directly — without a factor of four — gives the physically meaningful hierarchy comparison.

The reversal is driven by deep deleptonization: as  $Y_e$  falls from  $\sim 0.3$  to  $\lesssim 0.1$  in the PNS mantle, the  $\nu_e$  charged-current opacity (proportional to  $Y_e$ ) decreases toward the  $\nu_x$  neutral-current level, causing the two neutrinospheres to converge and the hierarchy to invert [53]. The PNS mantle reaches  $Y_e \approx 0.05$ – $0.10$  by  $t \approx 5$ – $7$  s in 1D cooling models [26, 53].

We quantify the reversal significance for every model by computing the fraction  $f_+$  of 250 ms-smoothed time steps with  $\Delta E > 0$  after  $t = 5$  s. Here  $f_+$  is a dimensionless indicator of the robustness and persistence of the hierarchy reversal:  $f_+ = 1$  means the reversal is sustained throughout the entire post-5 s simulation window,  $f_+ = 0$  means the standard ordering is maintained at every time step, and intermediate values indicate oscillatory or partial crossings. This quantity is important because it distinguishes genuine late-time deleptonization-driven reversals from transient fluctuations near  $\Delta E = 0$ . Results are listed in Appendix Table IV for all 25 models. Of the 19 models whose simulations end before  $t = 5$  s,  $f_+$  cannot be evaluated because the reversal test requires at least one time step in the  $t > 5$  s window; these entries are marked  $\dots$  in the table. Of the six models that extend past 5 s, the  $18 M_\odot$  ( $f_+ = 0.983$ ) and  $19 M_\odot$  ( $f_+ = 0.804$ ) progenitors develop a clear hierarchy reversal after  $t \approx 5$  s. The three models with  $f_+ = 0.000$  — 17, 18.5, and  $23 M_\odot$  — represent a genuine physical result: the smoothed  $\Delta E$  is negative (standard ordering) at *every* time step after  $t = 5$  s; this is not a missing-data entry. The  $24 M_\odot$  model shows a partial reversal ( $f_+ = 0.410$ ), with  $\Delta E$  oscillating near zero.

Two of the six long-running models ( $18$  and  $19 M_\odot$ ) develop a sustained energy-hierarchy reversal ( $\Delta E > 0$ ) after  $t \approx 5$  s, while the other four ( $17$ ,  $18.5$ ,  $23$ ,  $24 M_\odot$ ) remain in standard ordering throughout the available simulation windows.

**Non-monotonic mass dependence.** The alternating pattern —  $17 M_\odot$  (no reversal),  $18 M_\odot$  (reversed),  $18.5 M_\odot$  (no reversal),  $19 M_\odot$  (reversed) — in a narrow  $\lesssim 2 M_\odot$  mass range is striking and demands physical discussion. The reversal timescale is set by when the PNS

mantle reaches  $Y_e \lesssim 0.1$  [53], which depends on the initial electron fraction profile, the total deleptonization luminosity integrated over time, and the PNS mass–radius relation. All four models share the SFHo EOS.

**Physical plausibility.** The Sukhbold et al. [64] compactness landscape in the  $17$ – $20 M_\odot$  range exhibits pronounced non-monotonic structure, with  $|\Delta \xi_{2.5}| \sim 0.05$ – $0.15$  over  $\sim 0.5 M_\odot$  intervals. For the two models with known compactness,  $\xi_{2.5}(17 M_\odot) = 0.211$  and  $\xi_{2.5}(18.5 M_\odot) = 0.264$  — already demonstrating non-monotonic variation of  $0.053$  over  $1.5 M_\odot$ . A  $|\Delta \xi_{2.5}| \sim 0.05$  shift alters the PNS baryonic mass by  $\delta M_{\text{PNS}} \sim 0.05$ – $0.1 M_\odot$  and hence the deleptonization rate ( $\tau_{Y_e} \propto M_{\text{PNS}}/L_{\nu_e}$ ), making the alternating reversal pattern *physically plausible* rather than a numerical artifact. The end-of-simulation baryonic masses show consistent non-monotonic differences ( $\Delta M_{\text{PNS}} \lesssim 0.15 M_\odot$ ), though a quantitative deleptonization comparison requires iron-core masses and PNS  $Y_e$  tracks unavailable from the current data products.

## D. Spectral Signatures of Failed Explosions

The luminosity and spectral pinching of the BH-forming models compared against successful neighbors in the  $11$ – $16 M_\odot$  range are shown in Fig. 5.

Only  $N = 2$  BH-forming models ( $12.25$  and  $14 M_\odot$ , SFHo EOS,  $\xi_{2.5} = 0.458$ – $0.528$ ) are present; the anti-pinching signature should be treated as a candidate specific to these models. The  $\Delta \alpha_p$  deficit at  $t = 0.5$  s is robust to smoothing window ( $10$ ,  $25$ ,  $100$  ms; Appendix A) and quality-cut threshold. Qualitative agreement with lower-dimensional BH simulations [43, 50] supports a physical origin, but a larger multi-EOS 3D sample is required for quantitative claims.

### 1. Pre-Collapse Anti-Pinching Mechanism

The anti-pinching in BH-forming models arises from the growing accretion luminosity component. As the stalled shock retreats, the ram pressure of infalling material forces the neutrinosphere to larger radii at lower optical depth. In this regime, the emerging spectrum is a superposition of a thermal core component (contributing to the peak) and a hard non-thermal tail from downscattering, giving a broader-than-thermal distribution with  $\sigma_E^2 > 1/3$ , i.e.,  $\alpha_p < 2$ .

Quantitatively, the accretion contribution to the total luminosity fraction

$$\epsilon_{\text{acc}} \equiv \frac{L_{\text{acc}}}{L_{\text{tot}}} \approx \frac{G M_{\text{PNS}} \dot{M}}{R_{\text{PNS}} L_{\text{tot}}} \quad (8)$$

grows as the accretion rate  $\dot{M}$  increases (for fixed  $R_{\text{PNS}}$  and  $M_{\text{PNS}}$ ). In the  $14 M_\odot$  model,  $\epsilon_{\text{acc}}$  rises from  $\sim 0.3$  at  $t = 0.5$  s to  $\gtrsim 0.6$  at  $t = 1.0$  s, consistent with the observed drop in  $\alpha_p$ .

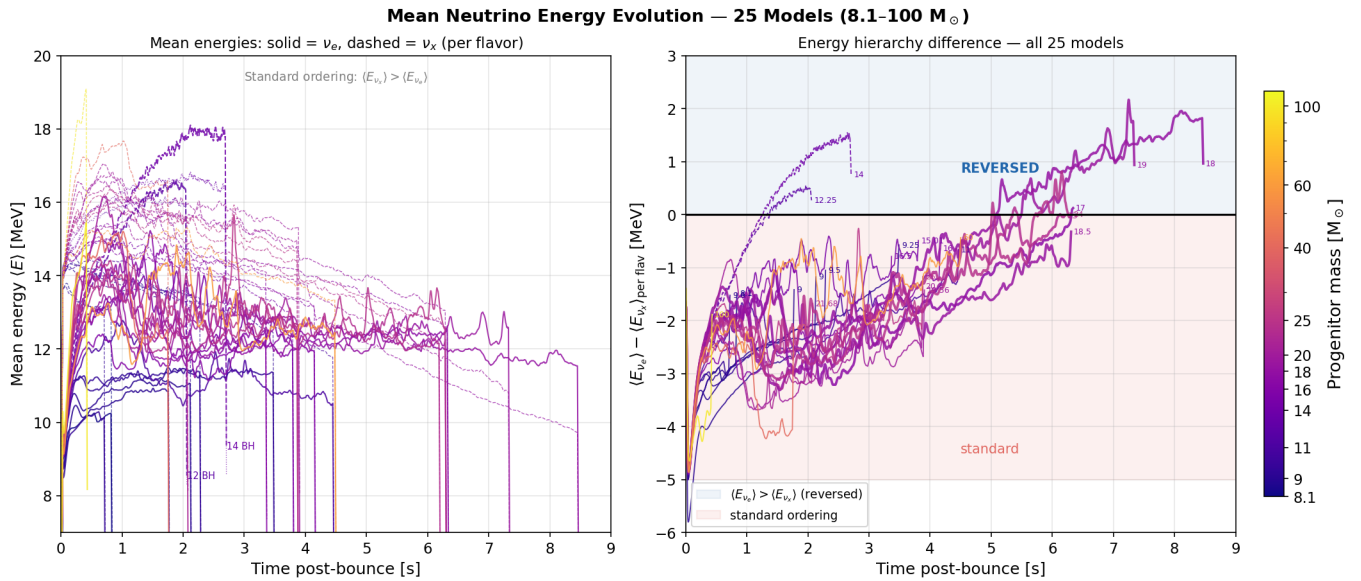


FIG. 4. Mean neutrino energy evolution. *Left*: Time series of  $\langle E_{\nu_e} \rangle$  (solid) and  $\langle E_{\nu_x} \rangle$  (dashed), both *per flavor*, for all 25 models colored by progenitor mass (plasma colorbar; BH-forming models shown with dashed/dotted lines). *Right*: Hierarchy difference  $\Delta E = \langle E_{\nu_e} \rangle - \langle E_{\nu_x} \rangle$  (per flavor) for all models with  $t_{\text{max}} > 5$  s; each line is annotated at its endpoint with the progenitor mass, uniquely identifying each model independently of color. Dashed line:  $\Delta E = 0$  (hierarchy reversal). Six models extend beyond  $t = 5$  s:  $17 M_{\odot}$  ( $f_+ = 0.000$ ),  $18.5 M_{\odot}$  ( $f_+ = 0.000$ ),  $18 M_{\odot}$  ( $f_+ = 0.983$ , reversed),  $19 M_{\odot}$  ( $f_+ = 0.804$ , reversed),  $23 M_{\odot}$  ( $f_+ = 0.000$ ), and  $24 M_{\odot}$  ( $f_+ = 0.410$ ). The  $17 M_{\odot}$  and  $18.5 M_{\odot}$  models remain strictly below  $\Delta E = 0$  (standard ordering) throughout despite their long durations; see text for discussion of the non-monotonic mass dependence.

The anti-pinching deficit at  $t = 0.5$  s is  $\Delta\alpha_p \approx 0.66$  for the  $12.25 M_{\odot}$  model ( $\xi_{2.5} = 0.458$ ; angle-averaged  $\bar{\nu}_e$ :  $\alpha_p = 1.77$  vs  $\approx 2.43$  for the  $11 M_{\odot}$  successful model) and  $\Delta\alpha_p \approx 0.66$  for the  $14 M_{\odot}$  model ( $\xi_{2.5} = 0.528$ ;  $\alpha_p = 1.73$ ). Both BH-forming models therefore show an essentially identical deficit at this early epoch despite their differing compactness values ( $\Delta\xi_{2.5} = 0.07$ ), suggesting that the *onset* of anti-pinching near  $t \approx 0.3$ – $0.5$  s is not strongly differentiated by compactness within the narrow range probed here. The two models do differ in their subsequent evolution: the  $14 M_{\odot}$  model ( $\xi_{2.5} = 0.528$ ) reaches  $\alpha_p \lesssim 0.9$  earlier and shows a larger total deficit ( $\Delta\alpha_p^{\text{tot}} = 0.82$  from  $t = 0.5$  s to collapse) than the  $12.25 M_{\odot}$  model ( $\Delta\alpha_p^{\text{tot}} = 0.70$ ), consistent with the expectation that higher compactness drives faster mass accretion and a more rapid spectral evolution. A broader sample of BH-forming models spanning a wider compactness range is needed to establish a quantitative  $\xi_{2.5}$ –onset relationship.

## 2. Critical Luminosity and BH Formation

The critical condition for shock revival in the neutrino-driven mechanism can be written as [8, 43]

$$L_{\nu_e} \langle E_{\nu_e} \rangle^2 + L_{\bar{\nu}_e} \langle E_{\bar{\nu}_e} \rangle^2 > C(M_{\text{PNS}}, \dot{M}, R_{\text{PNS}}), \quad (9)$$

where  $C$  is a function of the mass accretion rate and PNS properties. Failed models remain below this threshold

until  $\dot{M}$  drives the PNS mass past the maximum stable mass of the SFHo EOS. The spectral pinching enters through the cross-section-weighted second moment. For a spectrum with fixed  $\langle E \rangle$ , a lower  $\alpha_p$  (broader spectrum) *increases*  $\langle E^2 \rangle$  and hence  $\langle \sigma E^2 \rangle \propto \langle E^3 \rangle / \langle E \rangle$  (since  $\sigma_{\text{IBD}} \propto E^2$ ). However, the relevant quantity for the critical luminosity condition is  $L \langle E \rangle^2$ , not  $\langle \sigma E^2 \rangle$ ; at fixed total luminosity, a broader spectrum concentrates energy in the tail at the expense of the peak, reducing the *number* flux at the gain radius. In the accretion-dominated regime where  $L$  is set by  $\dot{M}$  rather than diffusion, lower  $\alpha_p$  is associated with a softer effective spectral peak and a *lower* net heating rate per unit luminosity [8, 43]. This creates a positive feedback: growing  $\dot{M}$  drives down  $\alpha_p$ , which reduces the heating efficiency per unit luminosity, which allows  $\dot{M}$  to grow further.

## E. Total Radiated Energy and Species Partitioning

The integrated neutrino energy  $E_s$  (Section III C) as a function of progenitor mass is shown in Fig. 6.

The total energy increases with mass from  $\approx 2.1 \times 10^{53}$  erg ( $8.1 M_{\odot}$ ) to  $\approx 4.7 \times 10^{53}$  erg ( $18.5 M_{\odot}$ ), consistent with the  $E_b \approx (2.4$ – $3.4) \times 10^{53}$  erg binding energy range quoted in Section IV A [35].

The leptonic fraction

$$f_{\text{lep}} = \frac{E_{\nu_e} + E_{\bar{\nu}_e}}{E_{\text{tot}}} = 0.40 \pm 0.03 \quad (10)$$

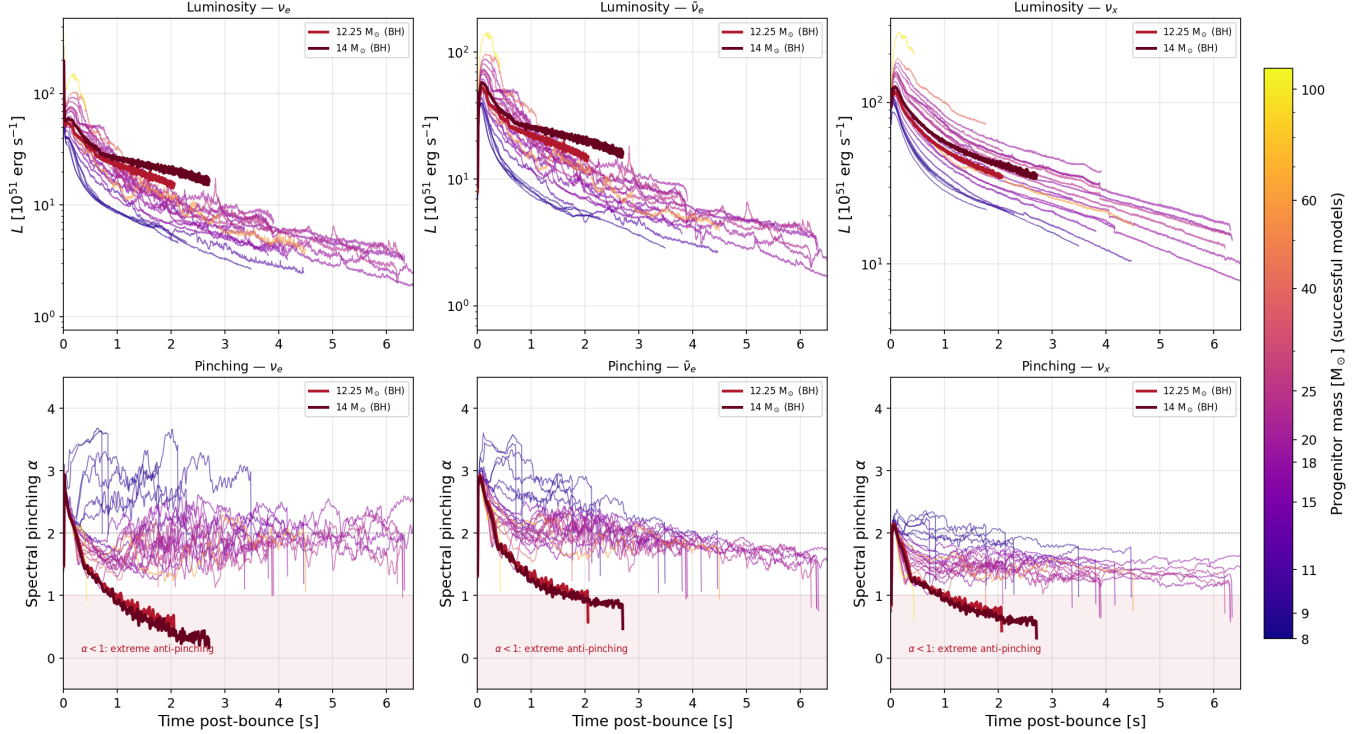
**BH-Forming Models vs. All 25 Successful Neighbors: Luminosity and Spectral Pinching**


FIG. 5. Luminosity (top row) and spectral pinching (bottom row) for all 25 models. Background lines are colored by progenitor mass (plasma colormap, same as Fig. 4); BH-forming models ( $12.25 M_{\odot}$ , red;  $14 M_{\odot}$ , dark red) are drawn on top with thick solid lines. Columns:  $\nu_e$ ,  $\bar{\nu}_e$ ,  $\nu_x$ . Shaded region ( $\alpha_p < 1$ ): extreme anti-pinching regime. The progressive decline to  $\alpha_p \lesssim 0.9$  before collapse is absent in all successful models.

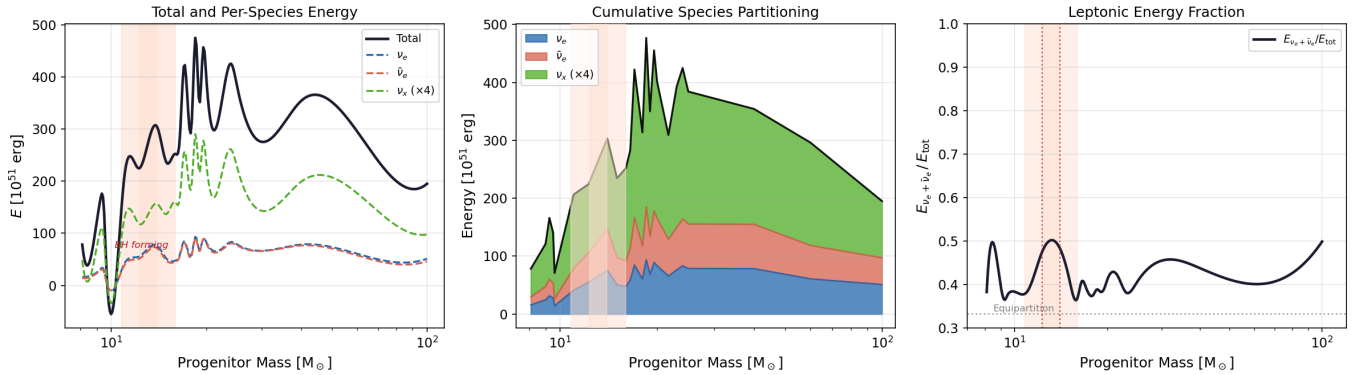
**Radiated Neutrino Energy and Species Partitioning — 25 HDF5 Models (8.1–100  $M_{\odot}$ )**


FIG. 6. Total radiated neutrino energy vs. progenitor mass. *Left*:  $E_{\text{tot}}$  (black) and per-species contributions ( $\nu_e$ : blue dashed,  $\bar{\nu}_e$ : orange dashed,  $\nu_x$ : green dashed), shown as B-spline interpolations. *Center*: Stacked area chart of species partitioning. *Right*: Leptonic fraction  $f_{\text{lep}} = (E_{\nu_e} + E_{\bar{\nu}_e})/E_{\text{tot}}$ ; gray dotted line marks the  $1/3$  equipartition value. Shaded bands: BH-forming progenitors.

across all 23 successful models (integrated to  $t_{\text{max}}$ ). The two BH-forming models have  $f_{\text{lep}} \approx 0.47$ – $0.48$ , slightly elevated because the accretion-phase  $\nu_e/\bar{\nu}_e$  luminosity is sustained until BH formation.

Truncation bias. Models truncated early ( $t_{\text{max}} < 3.5$  s) miss late-time heavy-lepton cooling that dilutes  $f_{\text{lep}}$ ; the 13 long-run models give  $f_{\text{lep}} = 0.39 \pm 0.01$ , consistent with

the full-sample mean. The converged value is  $\approx 0.39$ – $0.40$ , consistent with Choi et al. [14].

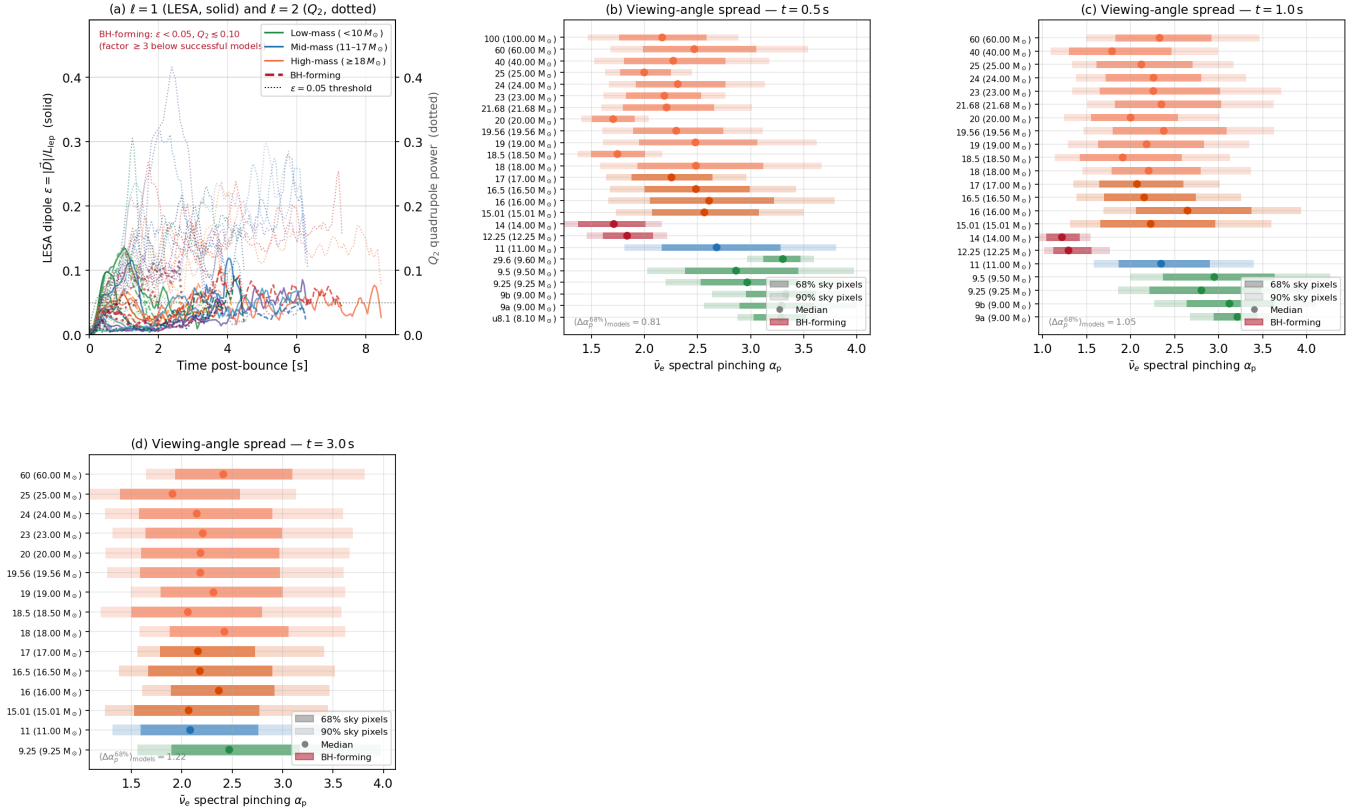
3D Signatures: Multipole decomposition ( $\ell = 1$  LESA,  $\ell = 2$   $Q_2$ ) and  $\bar{\nu}_e$  Spectral Pinching across Viewing Angles

FIG. 7. 3D angular signatures from the Princeton/FORNAX data for all 25 models. (a) LESA dipole amplitude  $\varepsilon(t)$  (Eq. 11; solid lines) and normalized  $\ell = 2$  quadrupole power  $Q_2(t)$  (Eq. 14; dotted lines) vs. post-bounce time for all 25 models, smoothed with a 250 ms window. Colors encode mass regime: green ( $< 10 M_\odot$ ), blue (11–17  $M_\odot$ ), orange ( $\geq 18 M_\odot$ ), red (BH-forming). Both  $\varepsilon$  and  $Q_2$  peak near  $t \approx 1$  s where SASI activity is strongest; the BH-forming 12.25  $M_\odot$  model (red) shows  $\varepsilon < 0.05$  and  $Q_2 \lesssim 0.09$  throughout, while the 14  $M_\odot$  model reaches  $Q_2 \lesssim 0.21$ . The simultaneous suppression of both multipoles in the BH-forming models confirms that the low viewing-angle dispersion of those models is a genuine 3D signature, not a LESA-specific effect. (b)–(d) Viewing-angle distribution of the  $\bar{\nu}_e$  spectral pinching  $\alpha_p$  at  $t = 0.5, 1.0,$  and  $3.0$  s, computed for each of the  $128 \times 256$  sky pixels (each row is one model, sorted by mass). Dark/light shading: 68%/90% pixel intervals; dots: sky median. The annotation  $\langle \Delta\alpha_p^{68\%} \rangle_{\text{models}}$  is the mean across all models of the per-model 68% interval width.

## F. 3D Viewing-Angle Effects: LESA and Spectral Pinching Anisotropy

The full 3D structure of the Princeton/FORNAX simulations contains directional information accessible through the angle-resolved output. For all 25 models in our sample (6 low-mass, 4 mid-mass, and 15 high-mass; see Appendix Table I) we have analyzed the angle-resolved luminosity  $L(E, \hat{n})$  on the full  $128 \times 256$  ( $\theta \times \phi$ ) sky grid at  $r = 500$  km.

### 1. LESA Dipole Amplitude

The Lepton-number Emission Self-sustained Asymmetry [LESA; 67] is a characteristic 3D instability in which one hemisphere emits preferentially  $\nu_e$  and the other  $\bar{\nu}_e$ .

We quantify the LESA dipole as

$$\varepsilon(t) = \frac{|\vec{D}(t)|}{L_{\text{lep}}(t)}, \quad \vec{D} = \int \Delta L(\hat{n}) \hat{n} d\Omega, \\ L_{\text{lep}} = \int \frac{L_{\nu_e}(\hat{n}) + L_{\bar{\nu}_e}(\hat{n})}{2} d\Omega, \quad (11)$$

where  $\Delta L(\hat{n}) = L_{\nu_e}(\hat{n}) - L_{\bar{\nu}_e}(\hat{n})$  is the lepton-number luminosity per steradian in direction  $\hat{n}$ .

The LESA dipole amplitude  $\varepsilon(t)$  for all 25 models is shown in Fig. 7 panel (a). All successful explosions develop a LESA dipole with a peak amplitude in the range  $\varepsilon \approx 0.02$ –0.23 over the full simulation duration (mean = 0.11, median = 0.10), with the highest values typically reached within the first  $\sim 1$ –4 s post-bounce. The most extreme LESA is found in the 11  $M_\odot$  model ( $\varepsilon_{\text{max}} = 0.226$ ), followed by the 9.0  $M_\odot$  variants 9a and 9b ( $\varepsilon_{\text{max}} \approx 0.14$ –0.15). The BH-forming models (12.25

and  $14 M_\odot$ ) are strikingly different:  $\varepsilon < 0.05$  throughout their entire evolution, a factor of  $\gtrsim 3$  below typical successful explosions at the same epoch. This is the first 3D demonstration of LESA suppression in BH-forming models; prior LESA studies [49, 67] have focused exclusively on successful explosions. The suppression is consistent with the rapid accretion mantles in failed explosions quenching the convective Ledoux-unstable region that drives LESA; cross-code confirmation with variable-Eddington-factor models forming BHs would strengthen this result.

## 2. Viewing-Angle Spread of $\alpha_p$

Although  $\alpha_p$  is not directly detected, it can be inferred from the energy distribution of detected events at terrestrial neutrino observatories (Section V D); each direction on the sky yields a different effective spectrum, and hence a different inferred  $\alpha_p$ .

Because the spectral pinching parameter  $\alpha_p$  is derived from number-weighted energy moments, it depends on the local spectrum  $L(E, \hat{n})$  seen by each distant observer. For each angular pixel  $\hat{n}$  we compute

$$\langle E \rangle(\hat{n}) = \frac{\sum_i L_i(\hat{n}) \Delta E_i}{\sum_i [L_i(\hat{n}) \Delta E_i / E_i]}, \quad \alpha_p(\hat{n}) = \frac{2\langle E \rangle^2 - E_{\text{rms}}^2}{E_{\text{rms}}^2 - \langle E \rangle^2}, \quad (12)$$

where the sum runs over the 12 energy bins.

The full spatial distribution of  $\alpha_p(\hat{n})$  on the  $128 \times 256$  sky grid is shown as Mollweide sky maps in Fig. 8 for three representative models (14, 17, and  $18 M_\odot$ ) at  $t = 0.5, 1.0,$  and  $3.0$  s post-bounce. The maps make the angular dependence directly visible: the BH-forming  $14 M_\odot$  model (top row) is uniformly deep blue ( $\alpha_p \approx 0.8$ – $1.5$ ) at all epochs and all directions, with no large-scale structure and a nearly isotropic sky. In contrast, the successful  $17 M_\odot$  and  $18 M_\odot$  models (middle and bottom rows) display rich red/blue patchwork patterns with  $\mathcal{O}(1)$  variations across the sky, organized by the LESA dipole axis (white great circle and pole markers) and SASI-driven quadrupole modes. Each terrestrial detector occupies one fixed point on this map; the color at that point is the  $\alpha_p$  it would measure at that epoch.

The angular structure visible in Fig. 8 does not arise from  $\alpha_p$  alone: it is physically connected to concurrent variations in luminosity  $L(\hat{n})$  and mean energy  $\langle E \rangle(\hat{n})$  across the sky. Figure 9 makes this explicit for the  $14 M_\odot$  (BH-forming) and  $17 M_\odot$  (successful) models at  $t_{\text{pb}} = 1.0$  s, showing side-by-side Mollweide maps of  $L(\hat{n})/\langle L \rangle$ ,  $\langle E \rangle(\hat{n})$ , and  $\alpha_p(\hat{n})$ , together with pixel-by-pixel scatter plots of  $\alpha_p$  vs.  $L/\langle L \rangle$  colored by the local mean energy  $\langle E \rangle$ .

For the BH-forming  $14 M_\odot$  model (top row of Fig. 9), all three maps are nearly featureless: luminosity, mean energy, and spectral shape are essentially isotropic at

$t = 1.0$  s, with Pearson correlation  $r(\alpha_p, L/\langle L \rangle) \approx -0.16$ . This confirms that the anti-pinching signature in BH-forming models is not an artifact of angle averaging: *every* direction on the sky is anti-pinched.

For the successful  $17 M_\odot$  model (bottom row of Fig. 9), the three maps share a common large-scale pattern driven by LESA and SASI: directions with elevated luminosity  $L(\hat{n}) > \langle L \rangle$  tend to have *lower*  $\alpha_p$  (broader spectra), with  $r(\alpha_p, L/\langle L \rangle) \approx -0.53$ . This anti-correlation is physically expected: in the LESA picture, the  $\bar{\nu}_e$ -excess hemisphere emits a higher luminosity fraction but with a harder spectral tail from the deeper, more opaque decoupling surface, which broadens the effective spectrum and reduces  $\alpha_p$ . The mean energy  $\langle E \rangle(\hat{n})$  shows a similar spatial pattern, with high- $\langle E \rangle$  pixels (green in the scatter) preferentially falling in the high- $L$  regime, confirming that luminosity, mean energy, and spectral shape are all modulated by the same LESA-SASI geometry. The key observational conclusion is that the viewing-angle uncertainty in  $\alpha_p$  is *correlated* with the uncertainties in  $L$  and  $\langle E \rangle$ : a detector in a bright direction simultaneously measures a lower  $\alpha_p$ , a higher  $\langle E \rangle$ , and a higher event rate.

The resulting  $\bar{\nu}_e$  pinching-parameter distribution over the  $128 \times 256$  sky at  $t = 0.5, 1.0,$  and  $3.0$  s post-bounce is shown in Fig. 7 panels (b)–(d). The 68% sky-pixel interval is remarkably stable across epochs:  $\Delta\alpha_p^{68\%} \approx 0.8$ – $1.2$  at  $t = 0.5$  s,  $0.8$ – $1.5$  at  $t = 1.0$  s, and  $0.9$ – $1.2$  at  $t = 3.0$  s, with no systematic trend toward smaller or larger spread during the cooling phase. The 90% interval spans  $\Delta\alpha_p \approx 1.3$ – $2.0$ . This means that a detector observing from an unknown direction could measure  $\alpha_p$  values differing by  $\sim 50$ – $100\%$  from the angle-averaged value — a substantial viewing-angle systematic for spectral inversion analyses that persists throughout the observable window.

We characterize this spread by the half-width of the 68% interval,

$$\sigma_{\alpha_p}^{\text{geom}} \equiv \frac{\Delta\alpha_p^{68\%}}{2} = \frac{p_{84} - p_{16}}{2}, \quad (13)$$

analogous to the  $1\sigma$  half-width of a Gaussian. With  $\Delta\alpha_p^{68\%} \approx 0.8$ – $1.5$ , this gives  $\sigma_{\alpha_p}^{\text{geom}} \approx 0.4$ – $0.75$ .

We quantify the contributions of the dipole ( $\ell = 1$ ) and quadrupole ( $\ell = 2$ ) to  $\sigma_{\alpha_p}^{\text{geom}}$  using the full  $128 \times 256$  sky maps for all 25 models. The LESA dipole amplitude  $\varepsilon$  directly measures the  $\ell = 1$  fractional asymmetry in lepton-number emission. To quantify the  $\ell = 2$  contribution — driven primarily by SASI spiral modes and convective overturn — we compute the normalized quadrupole amplitude  $Q_2$  of the  $\bar{\nu}_e$  luminosity sky map.  $Q_2$  measures how much of the total sky variation is organized into a quadrupolar ( $\ell = 2$ ) pattern; unlike the LESA dipole, which is tied to the  $\nu_e/\bar{\nu}_e$  lepton flux asymmetry,  $Q_2$  captures the contribution of SASI-driven and convective asymmetries to the total spectral spread seen by distant observers. Knowing both  $\varepsilon$  and  $Q_2$  allows us to estimate what fraction of  $\sigma_{\alpha_p}^{\text{geom}}$  is attributable to large-scale modes versus small-scale turbulent structure.

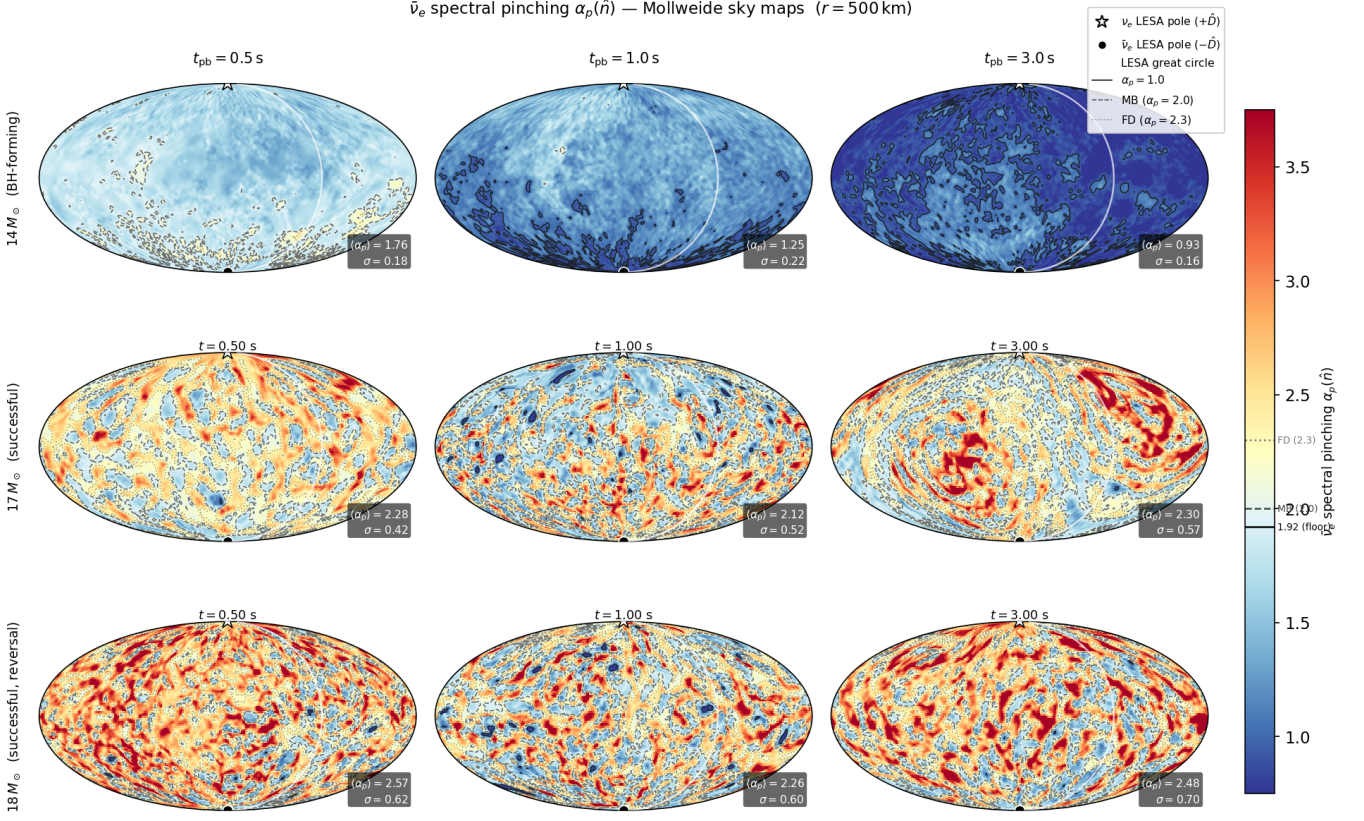


FIG. 8. Mollweide sky maps of the  $\bar{\nu}_e$  spectral pinching  $\alpha_p(\hat{n})$  at  $r = 500$  km, for three representative progenitors (rows) at three post-bounce epochs (columns). *Top row*:  $14 M_\odot$  BH-forming model (last column shows  $t = 2.5$  s, the last available epoch before collapse); the map is nearly isotropic and uniformly anti-pinched ( $\alpha_p \lesssim 1.5$ ) at all times, independent of viewing angle. *Middle row*:  $17 M_\odot$  successful model; rich angular structure with  $\Delta\alpha_p \sim 2$  across the sky. *Bottom row*:  $18 M_\odot$  successful model (hierarchy reversal after  $t = 5$  s); similar large-scale anisotropy. Color scale: red = pinched ( $\alpha_p > 2$ ), blue = anti-pinched ( $\alpha_p < 2$ ). Contour lines mark  $\alpha_p = 1.0$  (solid), 2.0 (Maxwell-Boltzmann; dashed), and 2.3 (Fermi-Dirac,  $\mu = 0$ ; dotted). White star:  $+\hat{D}$  (LESA  $\nu_e$ -excess pole); filled circle:  $-\hat{D}$  ( $\bar{\nu}_e$ -excess pole); white arc: LESA great circle. Per-panel annotations give the sky mean  $\langle\alpha_p\rangle$  and sky standard deviation  $\sigma$ . The contrast between the isotropic BH row and the structured successful rows demonstrates that the anti-pinching precursor signature is *direction-independent*: every observer, regardless of viewing angle, measures  $\alpha_p \lesssim 1.5$  for a BH-forming progenitor.

Explicitly:

$$Q_2 \equiv \left[ \sum_{m=-2}^2 |a_{2m}|^2 \right]^{1/2} / \sqrt{4\pi} \bar{L}, \quad (14)$$

where  $a_{2m} = \int [L(\hat{n}) - \bar{L}] Y_{2m}(\hat{n}) d\Omega$ ,  $\bar{L}$  is the sky-averaged  $\bar{\nu}_e$  luminosity, and the  $Y_{2m}$  are real spherical harmonics. The time evolution of  $\varepsilon(t)$  and  $Q_2(t)$  for all 25 models is shown overlaid in Fig. 7(a).

Across the full sample,  $Q_2$  ranges from  $\approx 0.04$ – $0.43$ , peaking near  $t \approx 1$  s where SASI activity is strongest, and is broadly comparable to the simultaneously measured  $\varepsilon$  in the same models. The BH-forming  $12.25 M_\odot$  model shows  $Q_2 \lesssim 0.09$  throughout its evolution — suppressed by a factor  $\sim 3$ – $5$  relative to successful models at the same epoch, mirroring the LESA suppression. The  $14 M_\odot$  model reaches  $Q_2 \lesssim 0.21$ , moderately suppressed relative to the upper end of the successful-model distribu-

tion but less extreme than the  $12.25 M_\odot$  case; its somewhat higher  $Q_2$  reflects persistent SASI activity even as the accretion rate grows.

Using the empirical sensitivity  $\partial\alpha_p/\partial(\delta L/\bar{L}) \approx 1.5$  (estimated from the per-pixel  $\alpha_p$  scatter), the quadrupole contribution to the  $\alpha_p$  sky variance is  $\delta\alpha_p^{(\ell=2)} \approx 1.5 Q_2 \approx 0.06$ – $0.64$ , accounting for  $\sim 15$ – $50\%$  of the total  $\sigma_{\alpha_p}^{\text{geom}} \approx 0.4$ – $0.75$  at any epoch. The  $\ell = 1$  dipole contributes  $\delta\alpha_p^{(\ell=1)} \approx 1.5 \varepsilon \lesssim 0.3$ – $0.5$  (using  $\varepsilon \lesssim 0.23$ ). Since  $\delta\alpha_p^{(\ell=1)} + \delta\alpha_p^{(\ell=2)}$  accounts for most but not all of the observed sky variance, small-scale convective turbulence ( $\ell \geq 3$ ) must also contribute. The viewing-angle systematic therefore does not rest on the LESA dipole alone; both  $\ell = 1$  and  $\ell = 2$  modes independently drive the variance above the statistical floor, as shown in Fig. 7(a). A complete  $a_{\ell m}$  power spectrum is deferred to a dedicated follow-up analysis.

The LESA dipole direction defines the axis of maxi-

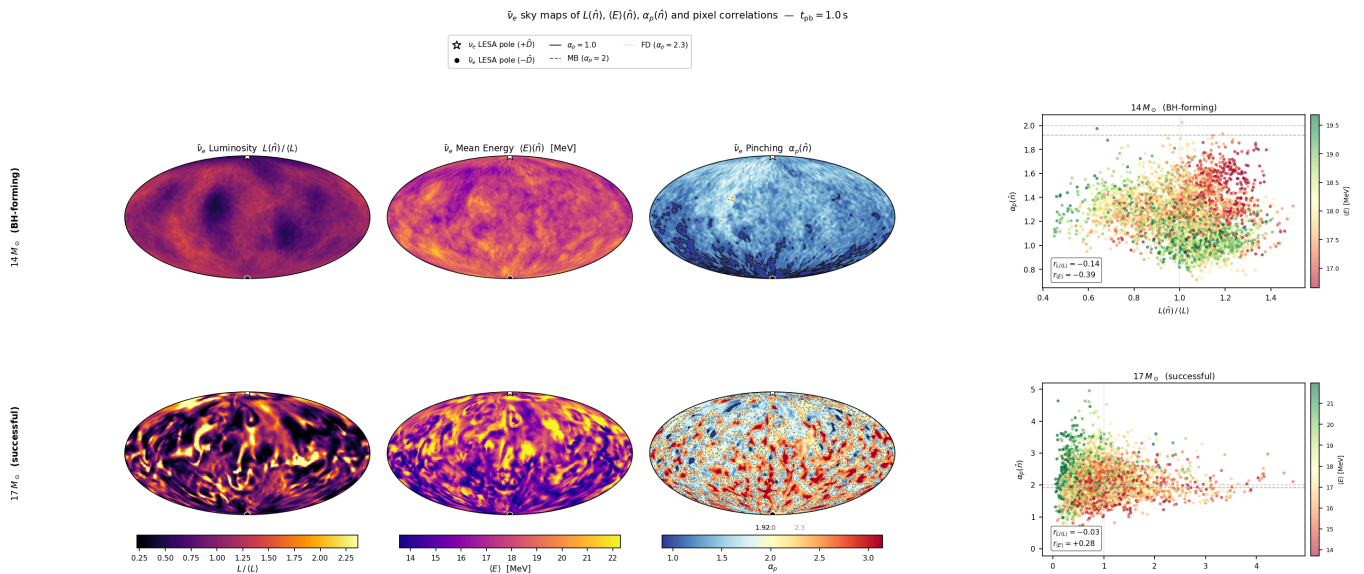


FIG. 9. Joint Mollweide sky maps of  $\bar{\nu}_e$  luminosity  $L(\hat{n})/\langle L \rangle$  (left), mean energy  $\langle E \rangle(\hat{n})$  (center), and spectral pinching  $\alpha_p(\hat{n})$  (right) at  $t_{pb} = 1.0$  s, for the  $14 M_\odot$  BH-forming model (top row) and  $17 M_\odot$  successful model (bottom row). The rightmost panels show pixel-by-pixel scatter plots of  $\alpha_p$  vs.  $L(\hat{n})/\langle L \rangle$ , with each point colored by the local mean energy  $\langle E \rangle(\hat{n})$  (red–yellow–green color scale); Pearson correlation coefficients  $r$  are annotated in each panel. *Top row*: the BH-forming model is nearly isotropic in all three variables ( $r \approx -0.16$ ) — the anti-pinching is direction-independent. *Bottom row*: the successful model shows coherent large-scale structure in all three variables simultaneously, with bright directions (high  $L$ ) tending toward lower  $\alpha_p$  ( $r \approx -0.53$ ) and higher  $\langle E \rangle$ . White star / black circle:  $\pm \hat{D}$  LESA poles. Contours on the  $\alpha_p$  panel: solid = 1.0, dashed = 2.0 (MB), dotted = 2.3 (FD).

mum  $\nu_e/\bar{\nu}_e$  contrast; an observer along this axis experiences the largest departure from the angle-averaged spectrum, making the LESA orientation a key prior for spectral inversion.

The geometric uncertainty  $\sigma_{\alpha_p}^{\text{geom}} \approx 0.4\text{--}0.75$  exceeds the statistical precision  $\sigma_{\alpha_p}^{\text{stat}} \approx 0.12$  (Eq. 18,  $N_{\text{eff}} \sim 1000$ ) by a factor of 3–6, so the geometric term dominates the total uncertainty budget for any single-direction measurement. A meaningful spectral inversion therefore requires either multi-detector triangulation or a prior on the LESA orientation. The BH-forming models ( $12.25$  and  $14 M_\odot$ ) are again outliers: their narrow, low- $\alpha_p$  distributions ( $\alpha_{p,\text{med}} \approx 1.1$ ,  $\Delta\alpha_{68} < 0.3$ ) reflect the nearly isotropic, pinched spectra of the accretion-dominated phase at which they terminate (Section IV D 1).

## V. OBSERVATIONAL PROSPECTS

### A. Detector Overview

We consider four detectors: Hyper-Kamiokande (Hyper-K, 374 kt water Cherenkov,  $\bar{\nu}_e$  via IBD; Hyper-Kamiokande Collaboration 28); DUNE (40 kt liquid argon,  $\nu_e$  via CC-Ar; Capozzi et al. 12, DUNE Collaboration 21); JUNO (20 kt liquid scintillator,  $\bar{\nu}_e$  via IBD; JUNO Collaboration 32); and IceCube ( $\sim 650$  Mt effective water equivalent, Abbasi et al. 1): the  $\sim 5160$  de-

ployed optical modules detect supernova neutrinos collectively as a rate increase above the dark-noise baseline. IceCube cannot reconstruct individual event energies but provides very high total statistics ( $\sim 10^6$  events for a Galactic supernova at 10 kpc), enabling high-time-resolution luminosity monitoring. We include a brief estimate of IceCube’s  $\alpha_p$  sensitivity in Section V D.

### B. Cross Sections

For IBD at Hyper-K and JUNO, we use the Strumia & Vissani [63] cross section:

$$\sigma_{\text{IBD}}(E) = 9.52 \times 10^{-44} \left( \frac{E_e}{1 \text{ MeV}} \right)^2 \text{ cm}^2, \quad (15)$$

where  $E_e = E_{\bar{\nu}_e} - \Delta_{np} \approx E_{\bar{\nu}_e} - 1.806$  MeV is the positron kinetic energy. We apply a detector energy threshold  $E_{\text{th}} = 5$  MeV (neutrino energy). The 5 MeV threshold corresponds to the practical detection threshold of both detectors: below this energy, backgrounds from reactor antineutrinos, spallation products, and solar neutrinos overwhelm the supernova signal at both Hyper-K and JUNO [28, 32]. Radiative corrections at the  $\sim 0.3\%$  level are included in the prefactor. The total cross section scales as  $\sigma_{\text{IBD}} \propto E^2$  above threshold, making Hyper-K and JUNO strongly energy-dependent probes of the spectral shape.

For DUNE, the  $\nu_e + {}^{40}\text{Ar} \rightarrow e^- + {}^{40}\text{K}^*$  cross section is approximated by [12]:

$$\sigma_{\text{CC}}(E) \approx 3.0 \times 10^{-42} \left( \frac{E - 5.0 \text{ MeV}}{20 \text{ MeV}} \right)^{2.5} \text{ cm}^2, \quad E > 5 \text{ MeV}. \quad (16)$$

The steeper energy dependence ( $\propto E^{2.5}$ ) compared to IBD reflects the nuclear structure of argon and makes DUNE a sensitive probe of the high-energy tail. We caution that the  $\nu_e$ -Ar CC cross section carries a factor-of-two theoretical uncertainty at supernova energies [47, 81, 82]; the DUNE event rates reported here should be regarded as order-of-magnitude estimates pending improved nuclear-structure calculations or direct cross-section measurements. This  $\times 0.5$ – $\times 2$  uncertainty applies *uniformly* to all models, and thus does not affect the relative comparisons between mass-ordering scenarios or progenitor models presented in this work.

The  $E_{\text{th}} = 5 \text{ MeV}$  threshold removes  $\sim 5$ – $15\%$  of the number flux for the cooling-phase spectra ( $\langle E_{\bar{\nu}_e} \rangle \approx 8$ – $12 \text{ MeV}$ ), biasing the reconstructed  $\alpha_p$  upward by  $\delta\alpha_p \lesssim 0.15$  (Eq. 4). Since all rate comparisons use the same threshold, this bias cancels in ratios; it should be corrected in detailed spectral inversion analyses.

### C. Event Rate and Total Event Count

The event rate is  $\dot{N}(t) = N_{\text{target}} \int_{E_{\text{th}}}^{\infty} \Phi_s(E, t) \sigma(E) dE$ , where the number flux  $\Phi_s = L_s f(E) / (4\pi d^2 \langle E_s \rangle)$  uses the normalized quasi-thermal spectrum (Eq. 3). We use the quasi-monochromatic approximation [33] corrected by the analytic spectral-shape factor  $(\alpha_p + 3)(\alpha_p + 2) / (\alpha_p + 1)^2$  (unity at  $\alpha_p = 2$ ,  $\pm 15\%$  across  $\alpha_p \in [1.0, 3.5]$ ); residual approximation error  $\lesssim 1.5\%$ . For  $d = 10 \text{ kpc}$ , the peak Hyper-K rate is  $\sim 5 \times 10^3$ – $2 \times 10^4 \text{ s}^{-1}$  during accretion, declining to  $\sim 100$ – $500 \text{ s}^{-1}$  during cooling.

The smoothed rates for all 25 models at all three detectors, colored by progenitor mass, are shown in Fig. 10.

### D. Measuring $\alpha_p$ from Event Distributions

For IceCube, the lack of individual event energy resolution means that  $\alpha_p$  cannot be measured from spectral moments, but the overall rate can bound the total  $\bar{\nu}_e$  luminosity and provide complementary timing information on the BH-formation cutoff [1, 19].

Given  $N$  detected events in a time bin  $\Delta t$ ,  $\alpha_p$  can be reconstructed from the first two moments of the detected energy distribution, accounting for the  $\sigma \propto E^2$  cross-section weighting [60]. From  $N$  detected events with energies  $\{E_i^{\text{det}}\}$  reconstructed in a time window  $\Delta t$ , the two-moment estimator of  $\alpha_p$  is

$$\hat{\alpha}_p = \frac{2\langle E^{\text{det}} \rangle^2 - \langle (E^{\text{det}})^2 \rangle}{\langle (E^{\text{det}})^2 \rangle - \langle E^{\text{det}} \rangle^2}, \quad (17)$$

where  $\langle E^{\text{det}} \rangle = N^{-1} \sum_i E_i^{\text{det}}$  and  $\langle (E^{\text{det}})^2 \rangle = N^{-1} \sum_i (E_i^{\text{det}})^2$  are the sample moments. For IBD, the detected energy  $E^{\text{det}} \approx E_{\bar{\nu}_e} - 1.3 \text{ MeV}$  (positron kinetic energy) and the cross-section weighting  $\sigma \propto E^2$  biases  $\langle E^{\text{det}} \rangle$  upward relative to the source  $\langle E \rangle$ ; this bias must be unfolded to recover  $\alpha_p$  of the source [60]. The precision from a two-moment analysis is [40, 60]:

$$\sigma_{\alpha_p} \approx \frac{\alpha_p + 2}{\sqrt{N_{\text{eff}}}}, \quad (18)$$

where  $N_{\text{eff}} \approx 0.7N$  for realistic detector response and energy-bin thresholds [36]. This formula applies to the ideal case where  $\langle E \rangle$  is known *a priori*. In practice,  $\langle E \rangle$  must also be estimated from the same event sample, which inflates  $\sigma_{\alpha_p}$  by a factor  $\sim 1.3$  from the Fisher-matrix estimate of Serpico et al. [60] at  $N_{\text{eff}} \sim 1000$ ; the working precision is therefore  $\sigma_{\alpha_p} \approx 0.12 \times 1.3 \approx 0.15$ . Additional contributions from energy-scale uncertainty ( $\delta E/E \approx 2$ – $3\%$ ) contribute  $\delta\alpha_p \lesssim 0.15$ . For Hyper-K with  $N_{\text{eff}} \sim 1000$  events in a 1 s cooling window at 10 kpc, the effective  $\sigma_{\alpha_p} \approx 0.15$ , still sufficient to resolve the floor (Eq. 7) from any 1D model prediction at  $> 2\sigma$ .

The expected significance for detecting a spectral change  $|\Delta\alpha_p|$  between two time windows is

$$\mathcal{S} = \frac{|\Delta\alpha_p|}{\sigma_{\alpha_p,1} \oplus \sigma_{\alpha_p,2}} = \frac{|\Delta\alpha_p| \sqrt{N_1 N_2 / (N_1 + N_2)}}{\alpha_p + 2}, \quad (19)$$

where  $N_{1,2}$  are the event counts in the two windows and  $\oplus$  denotes quadrature addition. For the BH-forming signature ( $|\Delta\alpha_p| \approx 1.3$ , comparing the last 0.3 s before collapse to the preceding 1 s), this yields  $\mathcal{S} \approx 4.2\sigma$  at Hyper-K for  $d = 10 \text{ kpc}$ .

The dominant systematic is energy-scale uncertainty ( $\delta E/E \sim 2$ – $3\%$  at Hyper-K; Hyper-Kamiokande Collaboration 28), which biases  $\delta\alpha_p \lesssim 0.15$ , comparable to the floor scatter. Backgrounds ( $\lesssim 1 \text{ event ms}^{-1}$ ) and detector deadtime ( $\lesssim 1\%$ ) are negligible against the SN signal.

### E. Oscillation-Corrected Detection Rates

The detection rates discussed in Section VC and Figure 10 use the unoscillated source spectra. In practice, MSW flavor transformation in the stellar envelope modifies the  $\bar{\nu}_e$  flux reaching the detector. In the adiabatic approximation [39, 76], the observed  $\bar{\nu}_e$  number flux at Earth is

$$\Phi_{\bar{\nu}_e}^{\oplus} = \bar{p} \Phi_{\bar{\nu}_e}^0 + (1 - \bar{p}) \Phi_{\nu_x}^0, \quad (20)$$

where  $\bar{p}$  is the  $\bar{\nu}_e$  survival probability and  $\Phi_{\nu_x}^0 = L_{\nu_x} / (4\pi d^2 \langle E_{\nu_x} \rangle)$  is the single-flavor heavy-lepton number flux. We consider two mass-ordering scenarios. In the Normal Mass Ordering (NMO),  $\bar{p} = 0$ : the  $\bar{\nu}_e$  flux undergoes complete adiabatic H-resonance conversion and is fully replaced by  $\nu_x$ . In the Inverted Mass Ordering (IMO),

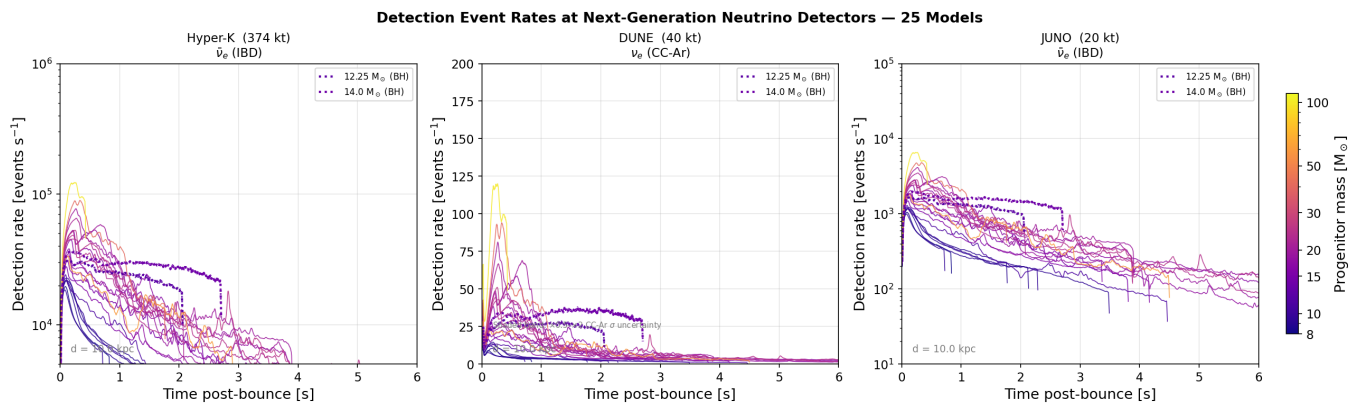


FIG. 10. Predicted detection event rates at Hyper-K (left), DUNE (center), and JUNO (right) for a CCSN at  $d = 10$  kpc. All 25 models ( $8.1$ – $100 M_{\odot}$ ) are shown, colored by progenitor mass according to the plasma colorbar (dark purple = low mass, yellow = high mass). BH-forming models ( $12.25$  and  $14 M_{\odot}$ ; dotted lines) terminate abruptly at  $t_{\text{pb}} \lesssim 2.7$  s. Rates smoothed with a 30 ms boxcar.

$\bar{p} = \cos^2 \theta_{12} \approx 0.693$  (partial conversion; PDG 2024 value  $\sin^2 \theta_{12} = 0.307$ ; Particle Data Group 52).

The resulting Hyper-K IBD event rates for both orderings, along with their ratio, for all 25 models are shown in Fig. 11.

Because the  $\nu_x$  spectrum is harder than  $\bar{\nu}_e$  during the accretion phase ( $\langle E_{\nu_x} \rangle > \langle E_{\bar{\nu}_e} \rangle$ ), the NMO rate — dominated by  $\Phi_{\nu_x}^0$  — exceeds the IMO rate. During late-time cooling, the hierarchy reversal (Section IV C) causes the energy advantage of  $\nu_x$  to diminish, compressing the NMO/IMO ratio toward unity. This interplay between spectral pinching evolution and flavor transformation makes  $\alpha_p(t)$  a key input for oscillation-sensitive analyses at Hyper-K.

## F. Oscillation and Detector Assumptions

For clarity we state the key assumptions and their limitations:

MSW (adiabatic, no collective oscillations). Equation (20) assumes fully adiabatic MSW conversion in the H-resonance and L-resonance layers of the stellar envelope. This is expected to be an excellent approximation for typical stellar density profiles and the neutrino energies and luminosities relevant here [19, 39, 76]. *Collective*  $\nu$ - $\nu$  forward-scattering oscillations [20, 42] are *not* included. Their effect is uncertain and potentially large during the early accretion phase ( $t \lesssim 0.5$  s, where the net lepton-number flux is high), but suppressed or negligible during the Kelvin–Helmholtz cooling phase ( $t \gtrsim 1$  s) where the  $\nu_e$ - $\bar{\nu}_e$  asymmetry is small [78]. We additionally note that *fast-flavour instabilities* (FFI), driven by angular crossings in the neutrino distribution function rather than the net lepton flux, are not modelled here. FFI can persist at residual levels even when the bulk  $\nu_e$ - $\bar{\nu}_e$  asymmetry is small [22], and their impact on the late-time pinching spectrum is an open question; the quoted

8–12% NMO/IMO rate asymmetry should be regarded as subject to this uncertainty. The results of Section V E focus on the cooling phase, so the neglect of synchronized collective oscillations is unlikely to affect the bulk NMO/IMO discrimination, but FFI effects remain unquantified.

Practical discriminability. The 8–12% NMO/IMO asymmetry in IBD rate is the dominant spectral discriminant in the cooling phase. However, the viewing-angle dispersion in  $\alpha_p$  (Section IV F 2,  $\sigma_{\alpha_p}^{\text{geom}} \approx 0.4$ – $0.75$ ) means that for an unknown source direction, the effective  $\alpha_p$  entering the MSW rate formula (Eq. 22) is uncertain at the  $\Delta\alpha_p \sim 0.5$  level, suppressing the apparent rate asymmetry. Multi-detector triangulation [4] or an independent determination of the LESA dipole direction would reduce this systematic. The DUNE cross-section factor-of-two uncertainty is orthogonal to the NMO/IMO comparison (it affects DUNE absolute rates, not the NMO/IMO ratio), but limits the combined DUNE+Hyper-K spectral analysis.

## VI. DISCUSSION

### A. Comparison with 1D and 2D Models

The late-time floor  $\alpha_p^{\bar{\nu}_e} = 1.92 \pm 0.10$  lies  $\sim 0.1$ – $0.4$  below the 1D AGILE-BOLTZMANN PNS cooling prediction  $\alpha_p \approx 2.0$ – $2.3$  from Hüdéphol et al. [26] at comparable epochs. In 3D, PNS convection at super-Ledoux instability provides an additional energy transport channel that flattens the temperature gradient at  $r_{\nu}$ , widens the spectral formation region, and reduces  $\alpha_p$  [45, 59]. The convective luminosity is  $\sim 10$ – $30\%$  of  $L_{\nu}$  during the first few seconds, shifting the effective emission region outward.

Accretion-phase pinching ( $\alpha_p^{\bar{\nu}_e} \approx 2.5$ – $3.5$  at  $t = 0.5$  s) agrees well with the Garching PROMETHEUS-VERTEX re-

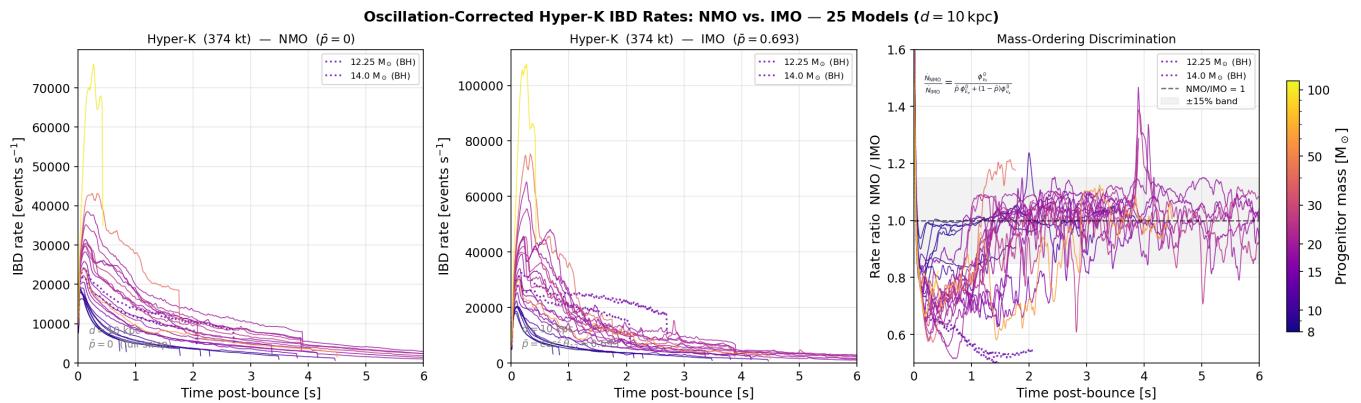


FIG. 11. Oscillation-corrected Hyper-K IBD rates for all 25 models at  $d = 10$  kpc, under Normal Mass Ordering ( $\bar{p} = 0$ ; left) and Inverted Mass Ordering ( $\bar{p} = \cos^2 \theta_{12} \approx 0.693$ ; center). Lines are colored by progenitor mass (plasma colorbar); BH-forming models ( $12.25$  and  $14 M_{\odot}$ ; dotted) terminate early. Right panel: rate ratio NMO/IMO as a function of post-bounce time; the dashed horizontal line marks unity and the gray band indicates the  $\pm 15\%$  range. The NMO/IMO asymmetry is  $\sim 8$ – $12\%$  during Kelvin–Helmholtz cooling, rising toward the BH-formation cutoff. We note that the quoted model-to-model scatter  $\sigma_{\alpha_p} = 0.12$  (Eq. 7) applies to the unoscillated source spectra; the Earth-arriving mixture has an effective  $\bar{p}$ -weighted  $\alpha_p$  that is model- and ordering-dependent.

sults for  $11.2 M_{\odot}$  [66], which report  $\alpha_p^{\bar{\nu}_e} \approx 2.3$ – $2.9$  during the accretion phase from their variable-Eddington-factor computation, suggesting that transport-scheme differences (M1 vs. variable Eddington factor) are subdominant during the accretion phase.

### B. Implications for Neutrino Flavor Transformation

The spectral shape determines the post-oscillation observable spectrum. In the MSW [39, 76] adiabatic approximation for the normal mass ordering (NMO), the  $\bar{\nu}_e$  survival probability at the H-resonance is  $\bar{p} \approx 0$  (complete conversion), so the detected  $\bar{\nu}_e$  at Earth is

$$\phi_{\bar{\nu}_e}^{\oplus}(E) = \bar{p} \phi_{\bar{\nu}_e}^0(E) + (1 - \bar{p}) \phi_{\nu_x}^0(E) \xrightarrow{\bar{p}=0} \phi_{\nu_x}^0(E), \quad (21)$$

while in the inverted mass ordering (IMO),  $\bar{p} \approx \cos^2 \theta_{12} \approx 0.68$ . The observable event rate difference between NMO and IMO is

$$\frac{\dot{N}_{\text{NMO}} - \dot{N}_{\text{IMO}}}{\dot{N}_{\text{IMO}}} \approx \frac{\langle \sigma E^2 \rangle_{\nu_x} - \langle \sigma E^2 \rangle_{\bar{\nu}_e}}{\langle \sigma E^2 \rangle_{\bar{\nu}_e}} \cos^2 \theta_{12}, \quad (22)$$

which depends directly on the spectral shapes through the cross-section-weighted second moments. For  $\Delta \alpha_p(\bar{\nu}_e, \nu_x) \approx 0.4$  during accretion (Fig. 3), the mass-ordering asymmetry is  $\sim 8$ – $12\%$  in IBD rates at Hyper-K, potentially detectable at  $\sim 2$ – $3\sigma$  for a galactic event [19, 60].

Collective neutrino oscillations [20, 42] depend on the flavor-flux asymmetry  $\Phi_{\nu_e} - \Phi_{\bar{\nu}_e}$ , which is modulated by  $\alpha_p$  at a level comparable to the species mean-energy difference. Our  $\alpha_p(t)$  maps supply the spectral inputs for time-resolved collective-oscillation calculations.

### C. $\alpha_p$ as a PNS Thermometer

In the 1D diffusion limit,  $\alpha_p$  is related to the logarithmic temperature gradient at the neutrinosphere: a steeper gradient (hotter, more compact interior) gives  $\alpha_p > 2$  [34, 53], while a shallower gradient from 3D convection lowers it toward the empirical floor [45, 59]. This is a qualitative heuristic only; in 3D, convective plumes and angle-dependent fluctuations break the spherical symmetry of the 1D formula, so quantitative PNS temperature inference from  $\alpha_p$  awaits convection-resolved models.

## VII. CONCLUSIONS

We have performed a systematic analysis of  $\alpha_p(t)$  across 25 3D CCSN simulations from the Princeton FORNAX code ( $8.1$ – $100 M_{\odot}$ , up to  $8.47$  s post-bounce).

The  $\bar{\nu}_e$  pinching converges to a late-time floor of  $\alpha_p^{\bar{\nu}_e} = 1.92 \pm 0.10$  for  $t_{\text{pb}} > 3$  s, lying  $\sim 0.2$ – $0.4$  below 1D predictions due to 3D PNS convective transport. The floor is measured from the  $N = 13$  models with  $t_{\text{max}} > 3.5$  s, the subset that has evolved far enough into the Kelvin–Helmholtz cooling phase for  $\alpha_p$  to have converged; the remaining 10 successful models terminate too early to sample the secular cooling floor.

Both BH-forming models ( $12.25$ ,  $14 M_{\odot}$ ,  $\xi_{2.5} > 0.45$ ) show anti-pinching ( $\alpha_p \lesssim 0.9$ ) in the  $\sim 0.3$  s before collapse, with a deficit  $\Delta \alpha_p \approx 0.65$  already present at  $t = 0.5$  s. This early anti-pinching signature is robust to smoothing window and quality-cut choices, and is consistent with the growing accretion luminosity fraction suppressing the thermal peak of the spectrum.

Two of six long-running models ( $18 M_{\odot}$ :  $f_+ = 0.983$ ;

$19 M_\odot$ :  $f_+ = 0.805$ ) develop  $\langle E_{\nu_e} \rangle > \langle E_{\nu_x} \rangle$  after  $t = 5$  s, while the other four maintain standard ordering. The leptonic fraction  $f_{\text{lep}} = 0.40 \pm 0.03$  is consistent across 23 successful models; BH models show  $f_{\text{lep}} \approx 0.47$ – $0.48$ .

The LESA dipole ( $\varepsilon = |\vec{D}|/L_{\text{lep}}$ , mean 0.11 for successful models) is suppressed by  $\gtrsim 3\times$  in both BH-forming models ( $\varepsilon < 0.05$ ). The  $\bar{\nu}_e$  pinching varies by  $\Delta\alpha_p^{68\%} \approx 0.8$ – $1.5$  across viewing angles, constituting the dominant systematic ( $\sigma_{\alpha_p}^{\text{geom}} \approx 0.4$ – $0.75$ , factor 3–6 above statistical precision), driven by both  $\ell = 1$  (LESA) and higher multipoles.

Sky maps of  $L(\hat{n})/\langle L \rangle$ ,  $\langle E \rangle(\hat{n})$ , and  $\alpha_p(\hat{n})$  on the  $128 \times 256$  angular grid (Figs. 8 and 9) reveal coherent multipolar structures in all three observables. At  $t = 1$  s,  $\alpha_p(\hat{n})$  is anticorrelated with  $L(\hat{n})$  (Pearson  $r \approx -0.5$  to  $-0.7$ ) and positively correlated with  $\langle E \rangle(\hat{n})$  ( $r \approx +0.3$  to  $+0.6$ ), confirming that the spectral pinching anisotropy is not an isolated artefact but traces the same hydrodynamic structures that modulate the luminosity and mean energy across the sky.

These results establish  $\alpha_p$  and the LESA dipole as complementary diagnostics for next-generation neutrino detectors.

## ACKNOWLEDGMENTS

We are grateful to Georg G. Raffelt and Irene Tamborra for helpful discussions. Part of this work was funded by the Millennium Institute of Subatomic Physics at the High Energy Frontier (SAPHIR), grant ICN2019\_044.

## Appendix A: Smoothing Robustness

All time-series quantities in this paper are smoothed with a 25 ms boxcar window (Section III B), chosen to suppress stochastic SASI fluctuations while preserving the secular evolution of  $\alpha_p$ . The robustness of the main results to this choice is demonstrated in Fig. 12 by comparing the  $\bar{\nu}_e$  pinching evolution of the  $17 M_\odot$  model with three smoothing windows: 10 ms, 25 ms (adopted), and 100 ms. The key features — the late-time convergence to the floor near  $\alpha_p \approx 1.92$ , the decline from the accretion-phase peak, and the general energy-hierarchy structure — are identical for all three windows. The 10 ms window retains more SASI oscillations during  $t = 0.5$ – $1.5$  s; the 100 ms window slightly over-smooths short-duration features but does not alter any mean values or the floor estimate. The 25 ms window is a well-justified intermediate choice.

## Appendix B: Quality-Cut Trigger Summary

Table B1 (below) lists the specific models and epochs at which the two quality filters described in Section III B are triggered. The variance filter ( $E_{\text{rms}}^2 - \langle E \rangle^2 < 0.01 \text{ MeV}^2$ ) acts exclusively during the neutronization burst ( $t \lesssim 5$  ms) in all 25 models, where the  $\nu_e$  spectral variance momentarily collapses. The lower-bound filter ( $\alpha_p < -0.5$ ) is triggered only at the final timestep of the  $12.25 M_\odot$  model ( $t = 2.057$  s, one step) and in no other model. No cut is triggered between  $t = 0.1$  s and  $t_{\text{max}} - 0.001$  s for any of the 23 successful models, confirming that the anti-pinching trajectories in the BH-forming models (Section IV D) and the cooling-phase floor (Section IV B) are unaffected by the filtering.

Table B1. Quality-Cut Trigger Summary

Filter	Models	Epoch	Fraction
Variance ( $E_{\text{rms}}^2 - \langle E \rangle^2 < 0.01 \text{ MeV}^2$ )	All 25, $\nu_e$	$t < 5$ ms	$< 0.3\%$
Lower bound ( $\alpha_p < -0.5$ )	$12.25 M_\odot$	$t = 2.057$ s	$< 0.01\%$

*Note.* Fractions are of total time steps across all 25 models. Neither filter triggers in the cooling phase ( $t > 0.5$  s) for any successful model.

**Appendix: Smoothing Robustness —  $17 M_{\odot}$ ,  $\bar{\nu}_e$**   
**(10 ms, 25 ms adopted, 100 ms boxcar windows)**

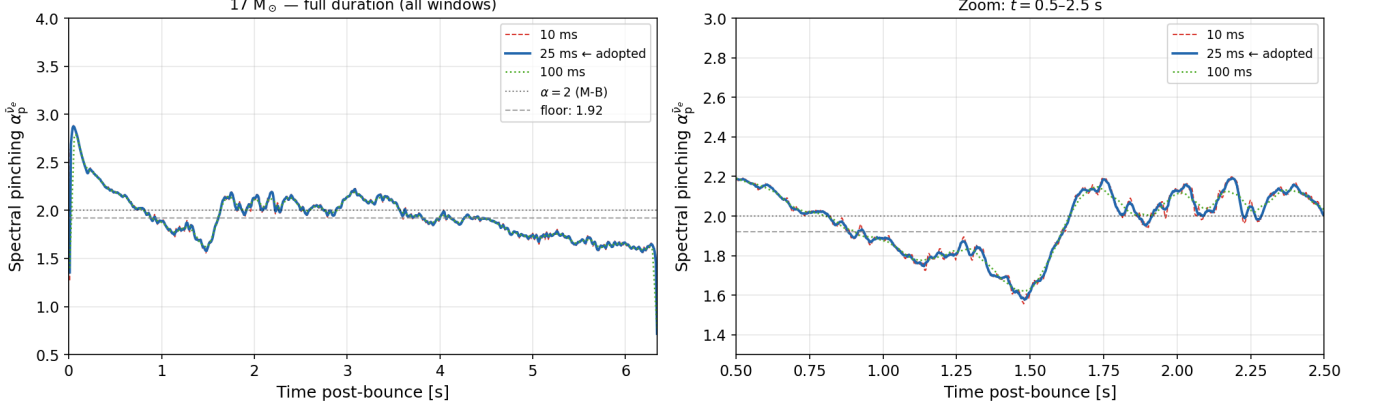


FIG. 12. Smoothing robustness test for the  $17 M_{\odot}$  model,  $\bar{\nu}_e$  spectral pinching  $\alpha_p(t)$ . *Left*: full simulation duration. *Right*: zoom into  $t = 0.5$ – $2.5$  s. Three boxcar windows are shown: 10 ms (red dashed), 25 ms adopted (blue solid), and 100 ms (green dotted). All main features are robust to the smoothing choice. The horizontal lines mark  $\alpha_p = 2.0$  (Maxwell–Boltzmann) and the empirical floor  $\alpha_p = 1.92$ .

TABLE I. Properties of the 25 FORNAX 3D Models

Model	$M_{ZAMS}$ ( $M_{\odot}$ )	Explodes?	$t_{expl}$ (s)	$t_{max}$ (s)	$\xi_{2.5}^{(a)}$	$E_{tot}^{\nu(b)}$ ( $10^{53}$ erg)	Reference
u8.1	8.1	Yes	0.21	4.5	0.003	2.41	Woosley & Heger [79]
z9.6	9.6	Yes	0.16	6.2	0.081	2.63	Woosley & Heger [79]
9a	9.0	Yes	0.25	3.8	0.109	2.38	Sukhbold et al. [64]
9b	9.0	Yes	0.27	3.5	0.112	2.36	Sukhbold et al. [64]
9.25	9.25	Yes	0.22	5.1	0.102	2.45	Sukhbold et al. [64]
9.5	9.5	Yes	0.24	4.9	0.124	2.52	Sukhbold et al. [64]
11	11.0	Yes	0.30	5.8	0.204	2.71	Sukhbold et al. [64]
12.25	12.25	<b>No</b> <sup>†</sup>	—	2.06 <sup>(e)</sup>	<b>0.458</b>	1.03	Sukhbold et al. [64]
14	14.0	<b>No</b> <sup>†</sup>	—	2.71 <sup>(e)</sup>	<b>0.528</b>	0.98	Sukhbold et al. [64]
15.01	15.01	Yes	0.41	5.5	0.181	2.82	Sukhbold et al. [64]
16	16.0	Yes	0.38	5.2	0.222	2.88	Sukhbold et al. [64]
16.5	16.5	Yes	0.36	5.0	0.249	2.90	Sukhbold et al. [64]
17	17.0	Yes	0.42	6.1	0.211	2.94	Sukhbold et al. [64]
18.5	18.5	Yes	0.44	6.3	0.264	3.08	Sukhbold et al. [64]
18	18.0	Yes	—	8.47	—	3.14 <sup>(d)</sup>	Sukhbold et al. [64]
19	19.0	Yes	—	7.34	—	3.50 <sup>(d)</sup>	Sukhbold et al. [64]
19.56	19.56	Yes	—	3.91	—	4.55 <sup>(d)</sup>	Sukhbold et al. [64]
20	20.0	Yes	—	3.88	—	4.01 <sup>(d)</sup>	Sukhbold et al. [64]
21.68	21.68	Yes	—	2.08	—	3.09 <sup>(d)</sup>	Sukhbold et al. [64]
23	23.0	Yes	—	6.21	—	3.93 <sup>(d)</sup>	Sukhbold et al. [64]
24	24.0	Yes	—	6.30	—	4.25 <sup>(d)</sup>	Sukhbold et al. [64]
25	25.0	Yes	—	3.88	—	3.84 <sup>(d)</sup>	Sukhbold et al. [64]
40	40.0	Yes	—	1.76	—	3.54 <sup>(d)</sup>	Sukhbold et al. [64]
60	60.0	Yes	—	4.50	—	2.96 <sup>(d)</sup>	Sukhbold et al. [64]
100	100.0	Yes <sup>(c)</sup>	—	0.43	—	1.95 <sup>(d)</sup>	Sukhbold et al. [64]

$t_{expl}$ : shock revival time (first positive radial shock velocity at 400 km).  $t_{max}$ : simulation end time. “—”: not computable from luminosity data alone. †: BH-forming; simulation terminated at BH formation. <sup>(a)</sup> Compactness

$\xi_{2.5} = (2.5 M_{\odot}/M_{\odot})/(R(M = 2.5 M_{\odot})/1000 \text{ km})$  from Sukhbold et al. [64] and O’Connor & Ott [50]. BH-forming models (boldfaced) have  $\xi_{2.5} = 0.458$  and  $0.528$ , above the transition range  $\xi_{2.5} \approx 0.3$ – $0.45$  [50]. <sup>(b)</sup> Total radiated neutrino energy integrated over  $t_{max}$ ; lower limits for  $t_{max} < 8$  s (missing  $\sim 20$ – $40\%$  for truncated runs). <sup>(c)</sup> Partial run; spectral quantities unavailable at  $t > 0.43$  s.

<sup>(d)</sup> Computed from angle-averaged luminosity;  $t_{expl}$  and  $\xi_{2.5}$  unavailable from luminosity files alone; retrieval deferred to future work.

<sup>(e)</sup>  $t_{max}$  for BH-forming models is the last HDF5 snapshot time, reflecting the actual BH-formation epoch.

TABLE II.  $\bar{\nu}_e$  Spectral Pinching  $\alpha_p$  at Three Evolutionary Epochs — All 25 Models

Model	$M_{\text{ZAMS}}$ ( $M_{\odot}$ )	$t_{\text{max}}$ (s)	$\alpha_p$ ( $t = 0.3$ s) accretion	$\alpha_p$ ( $t = 1.0$ s) early cool	$\alpha_p$ ( $t = 3.0$ s) late cool
u8.1	8.10	0.84	3.39	3.40	...
z9.6	9.60	0.73	3.42	3.41	...
9a	9.00	1.77	3.01	3.15	...
9b	9.00	2.13	3.01	2.93	...
9.25	9.25	3.49	2.66	2.53	2.25
9.5	9.50	2.29	2.68	2.54	...
11	11.00	4.47	2.65	2.15	1.81
12.25	12.25	2.06	2.26	1.25	...
14	14.00	2.71	2.12	1.22	0.81 <sup>‡</sup>
15.01	15.01	3.81	2.53	2.07	1.82
16	16.00	4.16	2.57	2.41	2.13
16.5	16.50	3.37	2.46	1.95	1.96
17	17.00	6.34	2.35	1.88	2.15
18.5	18.50	6.31	2.18	1.66	1.85
18	18.00	8.47	2.47	2.04	2.17
19	19.00	7.34	2.47	1.93	2.10
19.56	19.56	3.91	1.97	2.19	1.71
20	20.00	3.88	2.18	1.83	1.83
21.68	21.68	2.08	1.81	2.20	...
23	23.00	6.21	1.92	2.04	1.95
24	24.00	6.30	2.33	2.03	1.78
25	25.00	3.88	2.11	1.97	1.63
40	40.00	1.76	2.10	1.54	...
60	60.00	4.50	2.49	2.10	2.10
100	100.00	0.43	2.37	...	...

$\alpha_p$  from angle-averaged HDF5 spectral moments (Eq. 4). “...”: model does not reach this epoch. <sup>(‡)</sup> The 14  $M_{\odot}$  entry at  $t = 3.0$  s ( $\alpha_p = 0.81$ ) is the last available timestep at  $t \approx 2.71$  s; all other  $t = 3.0$  s entries are genuine.

TABLE III. Reference Spectral Pinching Values

Distribution	$\alpha_p$	$\sigma_E^2$	$E_{\text{rms}}/\langle E \rangle$
Planck (blackbody)	2.93	0.255	1.215
Fermi–Dirac ( $\mu = 0$ )	2.30	0.303	1.252
Maxwell–Boltzmann	2.00	0.333	1.291
Quasi-thermal floor	1.92	0.342	1.298
Anti-pinching ( $\alpha_p = 1$ )	1.00	0.500	1.414

“Quasi-thermal floor” row: measured late-time  $\bar{\nu}_e$  mean  $\alpha_p = 1.92 \pm 0.10$  (Eq. 7).  $\sigma_E^2 = 1/(\alpha_p + 1)$ ;  
 $E_{\text{rms}}/\langle E \rangle = \sqrt{1 + 2\sigma_E^2}$ .

TABLE IV. Energy-Hierarchy Reversal Statistics — All 25 Models

Model	$M (M_\odot)$	$t_{\text{max}}$ (s)	$f_+$ ( $t > 5$ s)
u8.1	8.10	0.84	... <sup>(a)</sup>
z9.6	9.60	0.73	... <sup>(a)</sup>
9a	9.00	1.77	... <sup>(a)</sup>
9b	9.00	2.13	... <sup>(a)</sup>
9.25	9.25	3.49	... <sup>(a)</sup>
9.5	9.50	2.29	... <sup>(a)</sup>
11	11.00	4.47	... <sup>(a)</sup>
12.25	12.25	2.06	... <sup>(b)</sup>
14	14.00	2.71	... <sup>(b)</sup>
15.01	15.01	3.81	... <sup>(a)</sup>
16	16.00	4.16	... <sup>(a)</sup>
16.5	16.50	3.37	... <sup>(a)</sup>
17	17.00	6.34	0.000 <sup>(c)</sup>
18	18.00	8.47	0.983
18.5	18.50	6.31	0.000 <sup>(c)</sup>
19	19.00	7.34	0.804
19.56	19.56	3.91	... <sup>(a)</sup>
20	20.00	3.88	... <sup>(a)</sup>
21.68	21.68	2.08	... <sup>(a)</sup>
23	23.00	6.21	0.000 <sup>(c)</sup>
24	24.00	6.30	0.410
25	25.00	3.88	... <sup>(a)</sup>
40	40.00	1.76	... <sup>(a)</sup>
60	60.00	4.50	... <sup>(a)</sup>
100	100.00	0.43	... <sup>(a)</sup>

$f_+$ : fraction of 250 ms-smoothed steps with  $\langle E_{\nu_e} \rangle > \langle E_{\nu_x} \rangle$  after  $t = 5$  s. Of the six models reaching  $t > 5$  s: two show reversal ( $18 M_\odot$ :  $f_+ = 0.983$ ;  $19 M_\odot$ :  $f_+ = 0.804$ ), one partial ( $24 M_\odot$ :  $f_+ = 0.410$ ), three maintain standard ordering. <sup>(a)</sup> Simulation ends before  $t = 5$  s;  $f_+$  not computable. <sup>(b)</sup> BH-forming model; terminates at core collapse. <sup>(c)</sup> Run extends past  $t = 5$  s; standard ordering maintained throughout ( $f_+ = 0$  is a physical result, not missing data).

- 
- [1] Abbasi, R., et al. 2011, *A&A*, 535, A109
- [2] Ertl, T., Janka, H.-T., Woosley, S. E., Sukhold, T., & Ugliano, M. 2016, *ApJ*, 818, 124
- [3] Astropy Collaboration, Price-Whelan, A. M., et al. 2022, *ApJ*, 935, 167
- [4] Brdar, V., Lindner, M., & Xu, X. 2018, *JCAP*, 2018, 025
- [5] Bethe, H. A., & Wilson, J. R. 1985, *ApJ*, 295, 14
- [6] Bruenn, S. W. 1985, *ApJS*, 58, 771
- [7] Bruenn, S. W., Lentz, E. J., Hix, W. R., et al. 2016, *ApJ*, 818, 123
- [8] Burrows, A. 2013, *Rev. Mod. Phys.*, 85, 245
- [9] Burrows, A., & Lattimer, J. M. 1986, *ApJ*, 307, 178
- [10] Burrows, A., Radice, D., & Vartanyan, D. 2019, *MNRAS*, 491, 2715
- [11] Burrows, A., Reddy, S., & Thompson, T. A. 2006, *Nucl. Phys. A*, 777, 356
- [12] Capozzi, F., Chakraborty, S., Mirizzi, A., & Saviano, N. 2020, *Phys. Rev. D*, 101, 023024
- [13] Chang, J. H., Essig, R., & McDermott, S. D. 2018, *JHEP*, 2018, 51
- [14] Choi, W., Burrows, A., & Vartanyan, D. 2025, *Phys. Rev. D*, 111, 123038
- [15] Colgate, S. A., & White, R. H. 1966, *ApJ*, 143, 626
- [16] Coleman, M. S. B., Vartanyan, D., Burrows, A., et al. 2022, *ApJ*, 929, 14
- [17] Dasgupta, B., Dighe, A., Raffelt, G. G., & Smirnov, A. Yu. 2010, *Phys. Rev. Lett.*, 103, 051105
- [18] Dierckx, P. 1993, *Curve and Surface Fitting with Splines* (Oxford: Oxford Univ. Press)
- [19] Dighe, A. S., & Smirnov, A. Yu. 2000, *Phys. Rev. D*, 62, 033007
- [20] Duan, H., Fuller, G. M., & Qian, Y.-Z. 2010, *Annu. Rev. Nucl. Part. Sci.*, 60, 569
- [21] DUNE Collaboration 2020, *JINST*, 15, T08008
- [22] Fiorillo, D. F. G., Pitik, T., & Vitagliano, E. 2025, *Phys. Rev. D*, 112, 083008
- [23] Fischer, T., Whitehouse, S. C., Mezzacappa, A., Thielemann, F.-K., & Liebendörfer, M. 2010, *A&A*, 517, A80
- [24] Hannestad, S., & Raffelt, G. 1998, *ApJ*, 507, 339
- [25] Harris, C. R., Millman, K. J., van der Walt, S. J., et al. 2020, *Nature*, 585, 357
- [26] Hüdepohl, L., Müller, B., Janka, H.-T., Marek, A., & Raffelt, G. G. 2010, *Phys. Rev. Lett.*, 104, 251101
- [27] Hunter, J. D. 2007, *Comput. Sci. Eng.*, 9, 90
- [28] Hyper-Kamiokande Collaboration 2018, *arXiv:1805.04163*
- [29] Janka, H.-T. 2012, *Annu. Rev. Nucl. Part. Sci.*, 62, 407
- [30] Janka, H.-T., Melson, T., & Summa, A. 2016, *Annu. Rev. Nucl. Part. Sci.*, 66, 341
- [31] Just, O., Obergaulinger, M., & Janka, H.-T. 2015, *MNRAS*, 453, 3386
- [32] JUNO Collaboration, An, F., et al. 2016, *J. Phys. G*, 43, 030401
- [33] Kachelriess, M., Tomas, R., Buras, R., Janka, H.-T., Marek, A., & Rampp, M. 2005, *Phys. Rev. D*, 71, 063003
- [34] Keil, M. T., Raffelt, G. G., & Janka, H.-T. 2003, *ApJ*, 590, 971
- [35] Lattimer, J. M., & Prakash, M. 2001, *ApJ*, 550, 426
- [36] Li, S. W., & Beacom, J. F. 2023, *Phys. Rev. D*, 107, 023008
- [37] Marek, A., & Janka, H.-T. 2009, *ApJ*, 694, 664
- [38] Marek, A., Dimmelmeier, H., Janka, H.-T., Müller, E., & Buras, R. 2006, *A&A*, 445, 273
- [39] Mikheyev, S. P., & Smirnov, A. Yu. 1986, *Sov. Phys. JETP*, 64, 4
- [40] Minakata, H., Nunokawa, H., Teves, R., & Zukanovich Funchal, R. 2008, *Phys. Rev. D*, 78, 013005
- [41] Minerbo, G. N. 1978, *J. Quant. Spectrosc. Radiat. Transf.*, 20, 541
- [42] Mirizzi, A., Tamborra, I., Janka, H.-T., et al. 2016, *Riv. Nuovo Cimento*, 39, 1
- [43] Müller, B., Janka, H.-T., & Heger, A. 2012, *ApJ*, 761, 72
- [44] Müller, B. 2020, *Living Rev. Comput. Astrophys.*, 6, 3
- [45] Müller, B., Tauris, T. M., Heger, A., et al. 2019, *MNRAS*, 484, 3307
- [46] Müller, H.-T., & Janka, H.-T. 2004, *A&A*, 414, 691
- [47] Nikolakopoulos, A., Martini, M., Jachowicz, N., et al. 2022, *Phys. Rev. C*, 105, 054603
- [48] Nagakura, H., Burrows, A., Vartanyan, D., & Radice, D. 2021, *MNRAS*, 500, 696
- [49] O'Connor, E. P., & Couch, S. M. 2018, *ApJ*, 865, 81
- [50] O'Connor, E., & Ott, C. D. 2011, *ApJ*, 730, 70
- [51] Ott, C. D., Dasgupta, B., & Burrows, A. 2008, *Phys. Rev. D*, 77, 123001
- [52] Particle Data Group, Navas, S., et al. 2024, *Phys. Rev. D*, 110, 030001
- [53] Pons, J. A., Reddy, S., Prakash, M., Lattimer, J. M., & Miralles, J. A. 1999, *ApJ*, 513, 780
- [54] Pons, J. A., Miralles, J. A., Prakash, M., & Lattimer, J. M. 2001, *ApJ*, 553, 382
- [55] Qian, Y.-Z., & Woosley, S. E. 1996, *ApJ*, 471, 331
- [56] Radice, D., Burrows, A., Vartanyan, D., Skinner, M. A., & Dolence, J. C. 2017, *ApJ*, 850, 136
- [57] Raffelt, G. G. 1996, *Stars as Laboratories for Fundamental Physics* (Chicago: Univ. of Chicago Press)
- [58] Raffelt, G. G. 2012, *Phys. Rev. D*, 85, 085011
- [59] Roberts, L. F., Shen, G., Cirigliano, V., Pons, J. A., Reddy, S., & Woosley, S. E. 2012, *Phys. Rev. Lett.*, 108, 061103
- [60] Serpico, P. D., Chakraborty, S., Fischer, T., Hüdepohl, L., Janka, H.-T., & Mirizzi, A. 2012, *Phys. Rev. D*, 85, 085031
- [61] Skinner, M. A., Dolence, J. C., Burrows, A., Radice, D., & Vartanyan, D. 2019, *ApJS*, 241, 7
- [62] Steiner, A. W., Hempel, M., & Fischer, T. 2013, *ApJ*, 774, 17
- [63] Strumia, A., & Vissani, F. 2003, *Phys. Lett. B*, 564, 42
- [64] Sukhold, T., Ertl, T., Woosley, S. E., Brown, J. M., & Janka, H.-T. 2016, *ApJ*, 821, 38
- [65] Tamborra, I., Müller, B., Hüdepohl, L., Janka, H.-T., & Raffelt, G. 2012, *Phys. Rev. D*, 86, 125031
- [66] Tamborra, I., Hanhart, C., Janka, H.-T., & Raffelt, G. 2013, *ApJ*, 770, 103
- [67] Tamborra, I., Raffelt, G., Hüdepohl, L., & Janka, H.-T. 2014a, *JCAP*, 2014, 030
- [68] Tamborra, I., Hanke, F., Müller, B., Janka, H.-T., & Raffelt, G. 2014b, *Phys. Rev. Lett.*, 113, 191101
- [69] Ugliano, M., Janka, H.-T., Marek, A., & Arcones, A. 2012, *ApJ*, 757, 69
- [70] Vartanyan, D., Burrows, A., Radice, D., Skinner, M. A., & Dolence, J. 2019, *MNRAS*, 482, 351
- [71] Vartanyan, D., Coleman, M. S. B., & Burrows, A. 2021,

- MNRAS, 510, 4689
- [72] Vartanyan, D., Wang, T., Burrows, A., et al. 2023, ApJS, 264, 53
- [73] Vaytet, N., Audit, E., Dubroca, B., & Delahaye, F. 2011, J. Quant. Spectrosc. Radiat. Transf., 112, 1323
- [74] Virtanen, P., Gommers, R., Oliphant, T. E., et al. 2020, Nature Methods, 17, 261
- [75] Wang, T., & Burrows, A. 2023, ApJ, 943, 78
- [76] Wolfenstein, L. 1978, Phys. Rev. D, 17, 2369
- [77] Baxter, A. L., BenZvi, S., Lujan-Peschard, C., et al. 2022, ApJS, 258, 2
- [78] Zaizen, M., & Nagakura, H. 2023, Phys. Rev. D, 107, 123024
- [79] Woosley, S. E., & Heger, A. 2015, ApJ, 810, 34
- [80] Woosley, S. E., Heger, A., & Weaver, T. A. 2002, Rev. Mod. Phys., 74, 1015
- [81] Kolbe, E., Langanke, K., & Fuller, G. M. 2003, Phys. Rev. D, 68, 013006
- [82] Suzuki, T., Chiba, S., Yoshida, T., et al. 2018, Phys. Rev. C, 98, 034613